JGR Earth Surface

Key Points:
- Comprehensive documentation of erosion and deposition along an active submarine normal fault scarp from the meter to submeter-scale
- Submarine erosion via earthquake-induced mass wasting may occur at similar rates to a variety of subaerial settings
- Process-based model for submarine scarp evolution with a threshold stability height of 20–40 m and a long-term average slope of 30°–40°

Supporting Information:
Supporting Information may be found in the online version of this article.

Correspondence to:
A. Hughes,
Hughes@ipgp.fr

Quantification of Gravitational Mass Wasting and Controls on Submarine Scarp Morphology Along the Roseau Fault, Lesser Antilles

Alex Hughes[1] , Javier Escartín[1,2] , Jean-Arthur Olive[2] , Jeremy Billant[3], Christine Deplus[1], Nathalie Feuillet[2], Frédérique Leclerc[3] , and Luca Malatesta[4]

[1]Institut de physique du globe de Paris, CNRS, Université de Paris, Paris, France, [2]Laboratoire de Géologie, Ecole Normale Supérieure (CNRS UMR,), PSL Research University, Paris 8538, France, [3]Université Côte d'Azur, CNRS, Observatoire de la Côte d'Azur, IRD, Valbonne, France, [4]GFZ German Research Center for Geosciences, Potsdam, Germany

Abstract Due to challenges involved in mapping the seafloor at high-resolution (e.g., <2 m), data are lacking to understand processes that control the evolution of submarine normal fault scarps, which cover large parts of the global seafloor. Here, we use data from autonomous deep-sea vehicles to quantify local erosion and deposition associated with a pronounced tectonic surface scarp formed by slip on the submarine Roseau normal fault (Lesser Antilles). We use high-resolution video imagery, photomosaics, and high-resolution bathymetric data (0.1–10 m/pixel) to identify active erosional features on the scarp including channels, steep gullies, small scarps, and debris cones. We compare volumes of erosion and deposition and find that under certain depositional conditions, debris cones effectively record the erosion signal of mass wasting from the footwall with a ratio of hanging wall deposition to footwall erosion of 0.80. We use eroded volumes to estimate earthquake-induced landslide erosion rates for the Roseau fault of 14–46 m Myr^{-1}. Assuming mass wasting of the Roseau fault scarp is mostly coseismic, the erosion rates for the Roseau fault imply that submarine earthquake induced mass-wasting can occur at similar rates to various terrestrial lithological and tectonic settings. We present a process-based model of submarine scarp degradation via retrogressive erosion in basement lithology where scarps have a gravitational stability threshold height of 20–40 m and a long-term average slope of 30°–40°. More generally, the results presented here may be applicable to develop models of submarine landscape evolution based on degradation of normal fault scarps on the seafloor.

1. Introduction

Understanding how tectonics and erosion shape the landscape is fundamental to infer deformation from geomorphic observables (e.g., Crosby & Whipple, 2006; Kirby & Whipple, 2012; Wobus et al., 2006). This is well-documented in extensional settings where slip on normal faults uplifts the surface, which is simultaneously or subsequently reworked by various erosive and sediment transport processes (e.g., Ellis et al., 1999; Jackson & White, 1989; Leeder & Gawthorpe, 1987). In terrestrial environments, first-order relationships that describe the changing morphology of the scarp during scarp growth have long been established (e.g., Wallace, 1977, 1978). Terrestrial scarp morphology is controlled by factors such as fluvio-glacial erosion (Sanchez et al., 2010; Tucker et al., 2011), hillslope diffusion (Pelletier et al., 2006; Petit & Mouthereau, 2012; Tucker et al., 2020), and landslides (Densmore et al., 1997, 1998). These different factors are routinely parameterized and incorporated into landscape evolution models that can be used to infer tectonic parameters such as scarp age and fault slip rate (Avouac, 1993; Petit et al., 2009; Phillips et al., 2003; Tucker et al., 2011).

For submarine environments, the factors that control scarp morphology are not well quantified because of a paucity of data that results from the challenging nature of collecting high-resolution (<2 m/pixel) bathymetric data from the seafloor. Collecting rock samples from the seafloor is also challenging and sparse sampling often hinders the construction of a high-resolution geochronology that can be used to constrain rates of tectonic or erosion processes. As a result, there are few data sets on fundamental metrics such as submarine scarp morphology (Armijo et al., 2005; Escartín et al., 2016; Hilley et al., 2020) and erosion rates (Marlow et al., 2000; Mitchell et al., 2003). Several factors that lead to continuous degradation of subaerial fault scarps, such as climatic weathering (e.g., freeze-thaw), rain splash, or overland flow do not

affect submarine fault scarps. Therefore, previous submarine erosion rates indicate that submarine erosion occurs either at slower rates than in subaerial settings (Marlow et al., 2000) or at rates similar to slowly eroding subaerial lowlands (Mitchell et al., 2003). The recent application of unmanned deep-sea vehicles, equipped with advanced acoustic and optical imaging technology, has provided researchers with the means to conduct bathymetric surveys at meter-scale resolutions. High-resolution bathymetric data sets are the key starting point from which to quantify parameters such as submarine erosion rates and to understand how tectonics, lithology, and erosion influence the evolution of submarine normal fault scarps. Quantification of the various parameters that control submarine normal fault scarp development is important because normal faults control topographic development for a large part of the global seafloor on abyssal plains.

Mass wasting is thought to be a key mechanism for erosion in submarine landscapes. A large body of work has focused on the mechanisms of submarine mass wasting and landslides in sediments on continental slopes (Coleman & Prior, 1988; Contreras-Reyes et al., 2016; Katz et al., 2015; Leynaud et al., 2009; Migeon et al., 2011; Mitchell, 2005; Mosher et al., 2004), in rift settings (Bilal et al., 2018; Elliott et al., 2012; Henstra et al., 2016; McLeod & Underhill, 1999; Stewart & Reeds, 2003), and in lacustrine settings (Moernaut et al., 2014; Strasser et al., 2006; Van Daele et al., 2015). At mid-ocean ridges, topographic development is mainly controlled by normal faults that expose basalt, gabbro, or ultramafic rocks on their footwall (Mitchell et al., 2000; Searle & Escartín, 2004) and submarine landslides or debris flows have been mapped at various scales from kilometers to the submeter scale (Cannat et al., 2013; Goff & Tucholke, 1997; McAllister & Cann, 1996; Tucholke, 1992; Tucholke et al., 1997). However, the role of surface processes, especially mass wasting, in the evolution of abyssal topography is poorly quantified. Few researchers (Cannat et al., 2013; Mitchell et al., 2000; Olive et al., 2019) have attempted to (1) quantitatively relate mass wasting and seismic activity at the scale of an individual submarine fault and (2) characterize the role of long-term fault slip rate, exposed lithology, chemical alteration, or magnitude-frequency distribution of earthquakes in the evolution of submarine fault scarp morphology. Consequently, we lack data on basic processes of erosion and deposition for a large portion of the global seafloor.

High-resolution bathymetric data have previously been used to study the fine morphology of active submarine fault scarps (e.g., Hilley et al., 2020), with some studies aiming to map the extent of recent coseismic ruptures (Armijo et al., 2005; Escartín et al., 2016). A link between footwall scarp degradation and fault growth has been suggested in rift-related sediments, whereby fault throw is thought to be the primary control on the size of erosional catchments in normal fault footwalls (Elliott et al., 2012). On transform faults in the Gulf of California, sediment fans and corresponding erosional features were identified in high-resolution bathymetric data and were interpreted to have formed synchronously during seismic shaking (Hilley et al., 2020). Furthermore, features such as rockslides (Cannat et al., 2013) and debris cones (Escartín et al., 2016) have previously been identified at the base of active submarine normal faults in volcanic bedrock. While these studies identified mass-wasted depositional features near the scarp, the precise link between mass wasting and scarp morphology on the scale of an individual submarine fault scarp remains understudied, especially in volcanic bedrock.

In this work, we use multiple high-resolution bathymetric and video-imagery data sets collected using underwater vehicles to describe the meter-scale morphology of a pronounced scarp associated with the Roseau normal fault in the Lesser Antilles volcanic arc (Figure 1). The Roseau fault flanks Les Saintes Islands (Figure 1) to the southwest. The fault is active and was the source of the 2004 M_w 6.3 Les Saintes earthquake (e.g., Bazin et al., 2010; Feuillet et al., 2011) that exhumed a ~1 m high coseismic band of fresh scarp (Escartin et al., 2016). A largely volcanic sequence is uplifting along the 160 m high (cumulative) Roseau fault scarp. The Roseau fault scarp dips to the N–NE and in the opposite direction to the regional slope, which deepens to the S–SW away from Les Saintes islands (Figure 2). These combined arguments make the Roseau fault scarp an excellent location to study small-scale mass wasting of submarine volcanic bedrock. Here, we quantify along-strike variations in the height, slope, and erosion of the scarp and assess the extent and volumes of a series of footwall catchments and associated debris cones to track spatial patterns of erosion and deposition. The detailed characterization of mass redistribution on an active submarine fault scarp informs our understanding of mass wasting processes and their impact on tectonic seascapes.
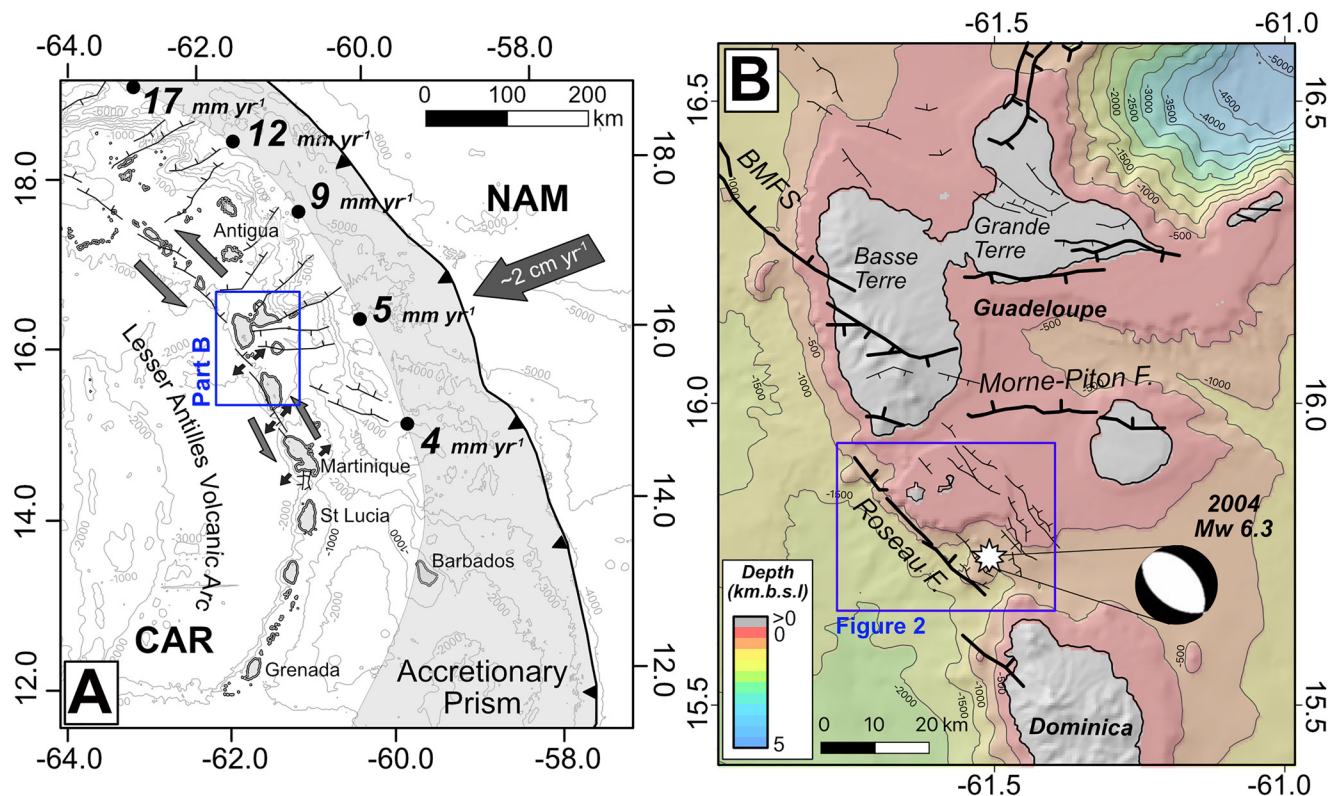
Figure 1. Tectonic and geographic setting of Les Saintes. Solid black lines are faults. (a) Tectonic setting of the Lesser Antilles volcanic arc adapted from Feuillet et al. (2011). The large arrow represents 2 cm yr^{-1} plate convergence between the North American plate (NAM) and the Caribbean plate (CAR) (DeMets et al., 2000; Dixon et al., 1998). Smaller gray arrows denote trench parallel shear which increases in magnitude north-westward (black dots and numbers) (López et al., 2006). Small black arrows denote extension. The light gray shaded area shows the extent of the accretionary prism. (b) Tectonic setting of Les Saintes and the Roseau fault adapted from Leclerc et al. (2016). Bathymetry is from the GEBCO grid (Weatherall et al., 2015). The white star and the beachball show the location and sense of slip for the 2004 Mw 6.3 Les Saintes earthquake (Bazin et al., 2010; Feuillet et al., 2011). BMFS: Bouillante-Montserrat Fault System, k.m.b.s.l = kilometers below sea level.

1.1. Tectonic Setting and Morphology of the Roseau Fault System

Oblique, NE–SW directed plate convergence at rates of ∼2 cm yr^{-1} causes subduction of the North American and South American plates beneath the Caribbean plate and is responsible for the formation of the Lesser Antilles volcanic arc (Figure 1a; Deng & Sykes, 1995; Feuillet et al., 2002, 2011; Jordan, 1975; Weber et al., 2001). Left-lateral transtensional deformation along the inner arc is partially accommodated by a right-stepping series of trench-parallel, en-échelon, oblique faults that generally trend between 130 and 160 degrees (Figure 1b; Feuillet et al., 2010, 2011). One such fault is the Roseau normal fault, which was the source of the damaging 2004 M$_w$ 6.3 Les Saintes earthquake and associated tsunami (Figure 1b; Bazin et al., 2010; Escartín et al., 2016; Feuillet et al., 2011; Le Friant et al., 2008; Salichon et al., 2009).

The ∼40 km long Roseau fault system forms the western boundary of the Les Saintes graben (Figure 2a). The Roseau fault system dips northeast and trends N140°E, crosscutting the seafloor along the southwest flank of the shallow Les Saintes reef plateau and the deeper Les Saintes Channel (Figure 2). The Roseau fault system has five individual segments (Sec Pâté, Canyon, Roseau, Le Havre, and Colibri), with pronounced scarps at the seafloor (Leclerc et al., 2016). The Canyon segment runs parallel to the southwestern edge of the Les Saintes reef plateau (Figure 2) and has a semi-continuous surface trace because the scarp is totally eroded within the main canyons carved into the western slope of the reef plateau (Leclerc et al., 2016). The left-stepping Le Havre and Colibri segments mostly uplift volcanic deposits on the southern flank of the Roseau volcano (Figure 2). For both segments, deformation is distributed among multiple scarps that vary in length from 100 m up to ∼2 km and reach heights approaching ∼100 m.
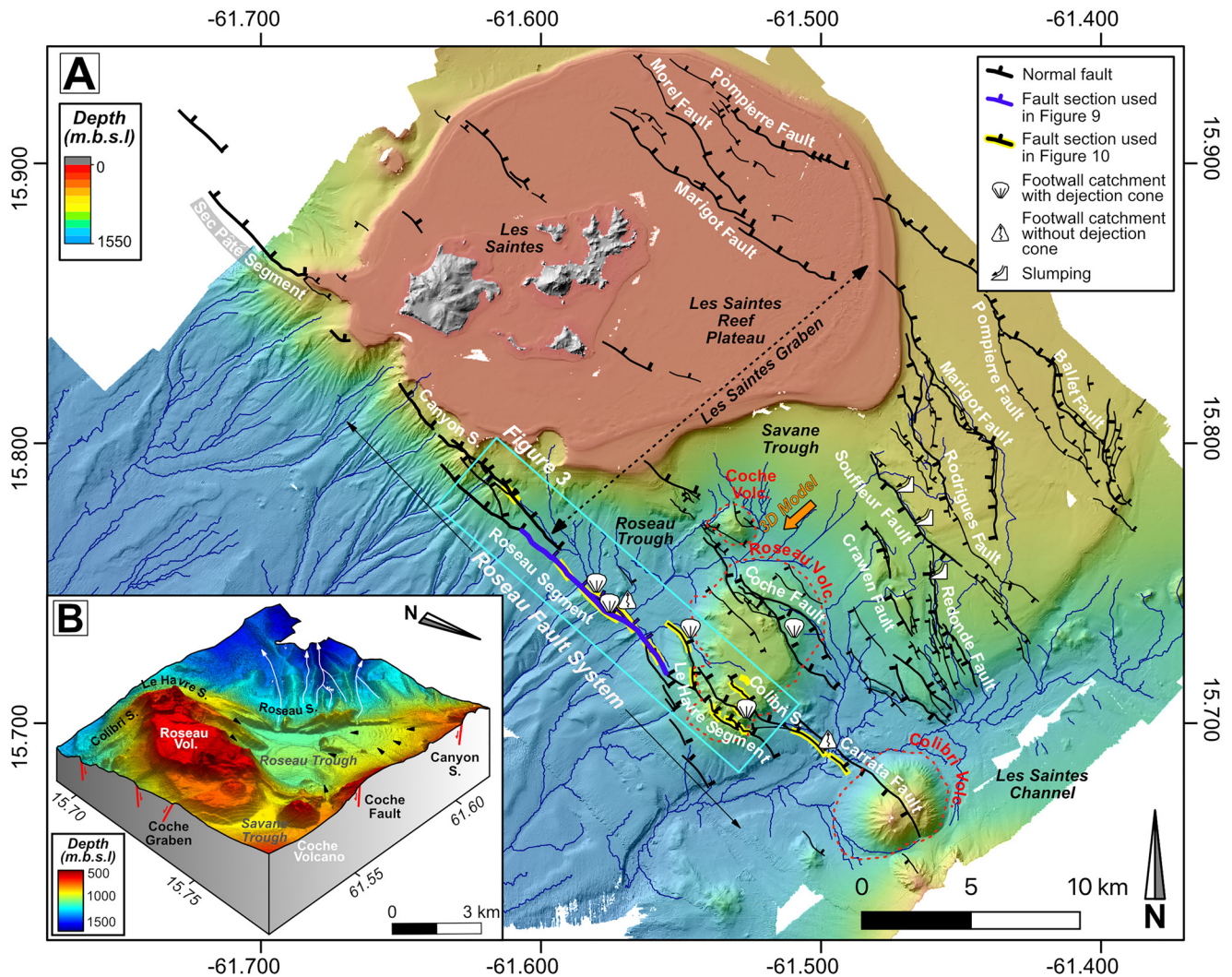
Figure 2. (a) Map of faults and volcanoes in the Les Saintes channel. Bathymetry data and shaded relief map are from the 10 m/pixel digital terrain model (DTM) (Leclerc et al., 2016). Normal fault traces (solid black lines) after Leclerc et al. (2016). Faults with the highest scarps are in bold and faults with thinner lines have lower scarp heights. The thin blue lines are the regional turbiditic channel network extracted from the 10 m/pixel DTM using TopoToolbox (Schwanghart & Scherler, 2014). The orange arrow shows the facing direction of B. (b) Three-dimensional block model showing sediment ponding in the Roseau trough due to uplift of the Roseau fault scarp (after Leclerc et al., 2016). Black triangles and white arrows show sediment transport directions.

The surface expression of the Roseau segment generally has a simple plan view morphology where deformation is focused on single fault strands with moderate scarp dip of around 30°–50° (Leclerc et al., 2016). In places, relay zones are formed by the overlapping sections at the ends of individual, left-stepping, en-echelon fault strands (Figure 3) and seismicity data indicate that the individual strands join to form a single fault plane at depth (Bazin et al., 2010). Along the Roseau segment, footwall erosion has incised a series of gullies and catchments in the highest sections of the footwall scarp, with debris cones forming at the mouth of individual gullies (Escartín et al., 2016).

Along the eastern side of the Les Saintes graben, west-dipping antithetic faults including the Souffleur, Redonde, and Rodrigues faults reach lengths up to 10 km and have maximum reliefs of ~150 m (Figure 2) (Leclerc et al., 2016). The Souffleur fault has a complex surface morphology with multiple steep lenses, slumps, and relays (Figure 2), which can approach slopes of 90° (Leclerc et al., 2016).
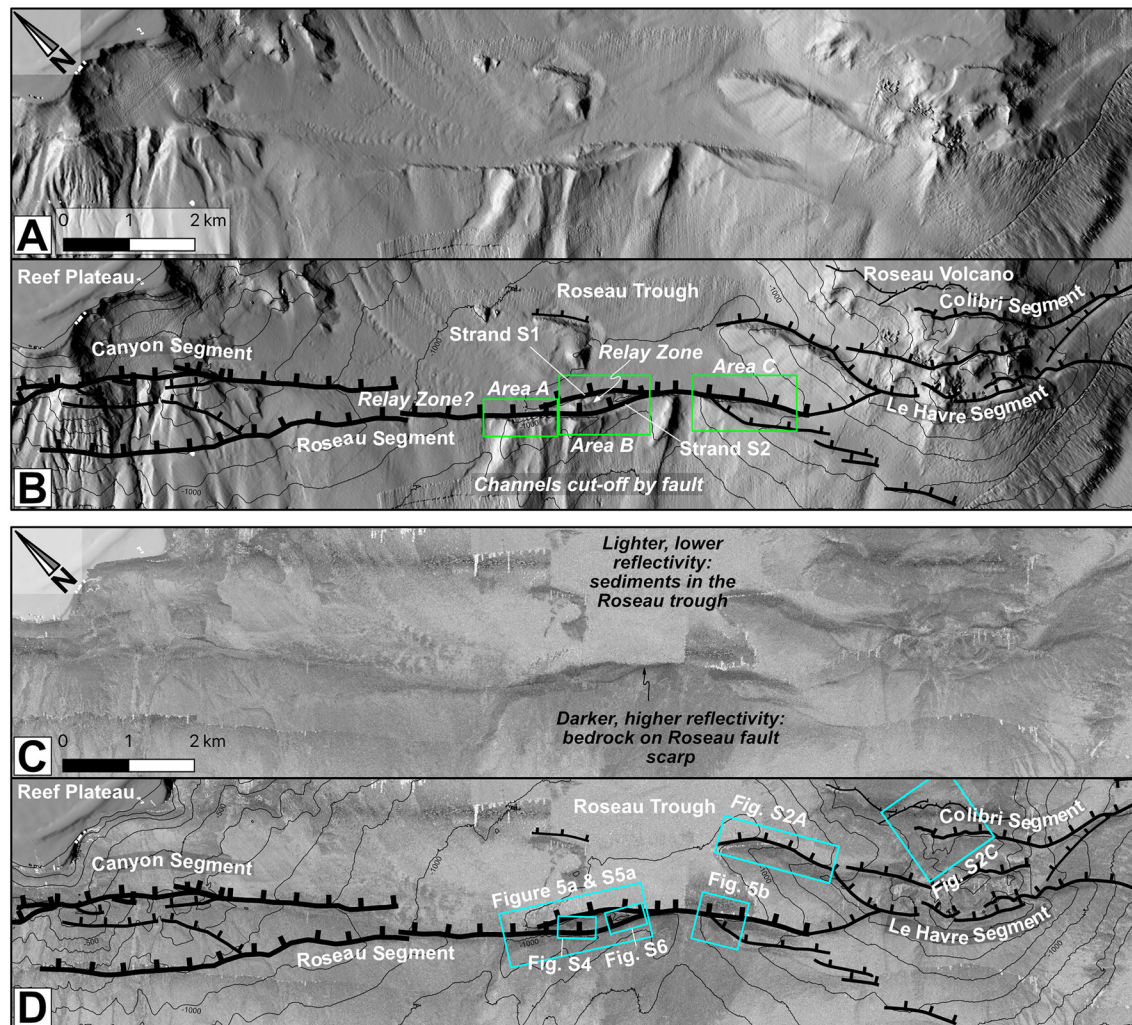
Figure 3. Surface morphology of the Roseau fault system. Figure located in Figure 2. (a) Shaded relief map of the Roseau fault system. (b) Same map as A with interpretation and the locations of areas A, B, and C referred to in the text (green boxes). (c) Backscatter map of the same area as part A showing the distribution of low reflectivity seafloor that we interpret to be sediments. We interpret dark, high-reflectivity seafloor to indicate volcanic basement, steep slopes, or rough seafloor resulting from either debris cones, rippled sediments, or scours from regional turbidity flows (Leclerc et al., 2016). (d) Same image as C with interpretation.

2. Data Sets

To document the decameter to submeter scale morphology of the Roseau fault and understand the extent to which mass-wasting processes control submarine scarp morphology, we conducted a comprehensive series of near-bottom high-resolution geophysical surveys at multiple scales (Figure 4). The main bathymetric and photographic data sets analyzed for this study were collected during the 2017 SUBSAINTES cruise (PI: J. Escartín, 2017; https://doi.org/10.17600/17001000) onboard the research vessel L'Atalante. We collected near-bottom high-resolution bathymetry data using the autonomous underwater vehicle (AUV) Aster[x] (IF-REMER, France) and we collected rock samples, still electronic images, and high-resolution video imagery using the remotely operated vehicle (ROV) Victor6000 (IFREMER, France). Data from the SUBSAINTES cruise were supplemented by previous shipboard multibeam bathymetric data obtained during the 2010 BATHYSAINTES cruise (PI: C. Deplus, 2010; https://doi.org/10.17600/10030020) conducted onboard the research vessel Pourquoi pas?. In 2013, the ODEMAR cruise (PI: Escartín and Andreani, 2013; https://doi.org/10.17600/13030070, research vessel: Pourquoi pas?) acquired high-resolution bathymetry and seafloor imagery with the AUV Abyss (GEOMAR, Germany) and ROV Victor6000. Additional details on these different data sets and their processing are provided in the supplementary material (Table S1).
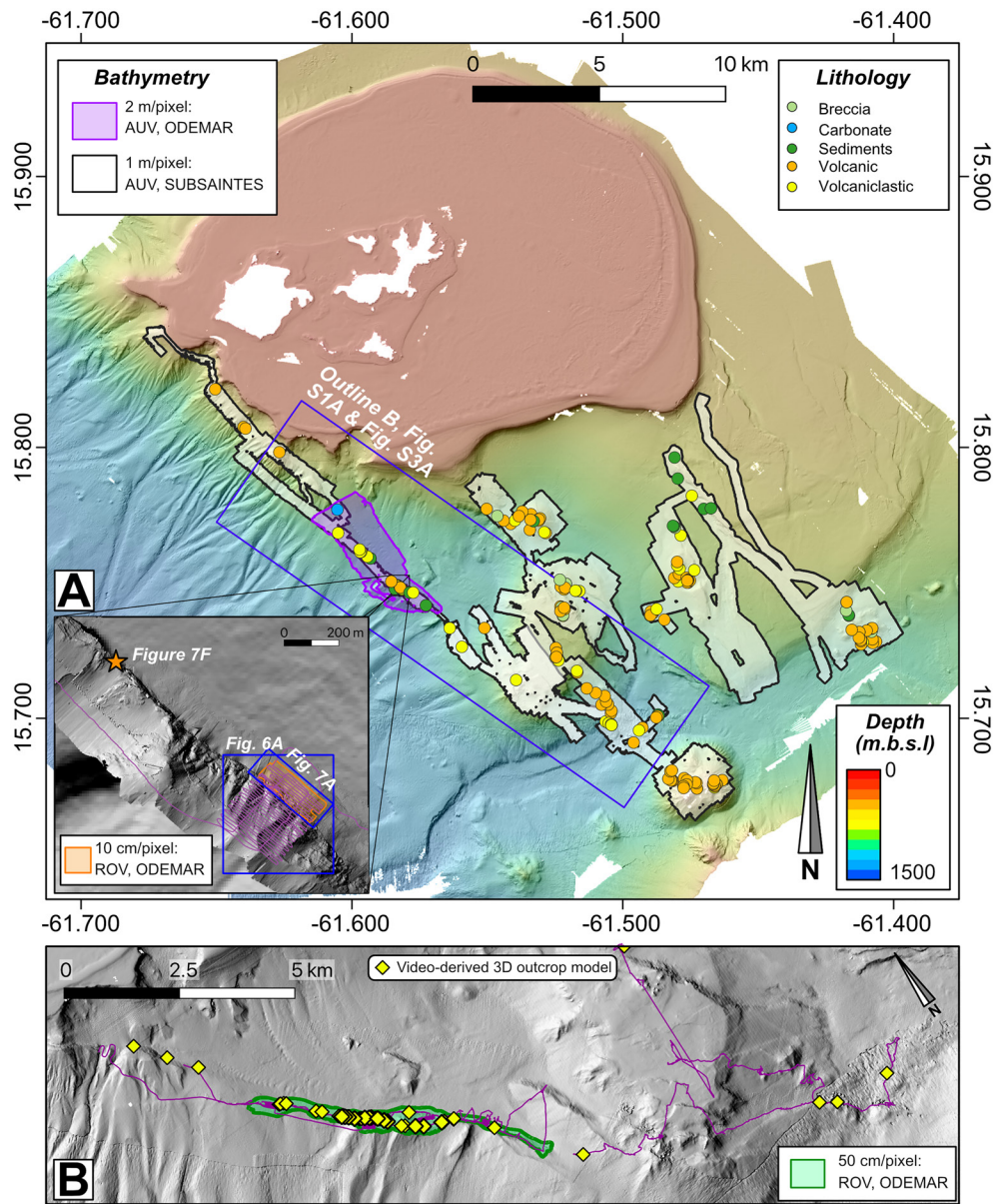
Figure 4. Data sets used to characterize the surface morphology of the western edge of Les Saintes graben. The extent of high-resolution bathymetry data is shown with the colored polygons overlain above a shaded relief map from the 10 m/pixel digital terrain model. The location of rock samples collected using a remotely operated vehicle (ROV) are shown with the colored circles. Inset (a) and part (b) Close up views showing the extent of bathymetry data gridded at 50 cm/pixel (part B) and 10 cm/pixel (inset A). ROV tracks are indicated with purple lines.

2.1. High-Resolution Bathymetry

We used various bathymetric data sets to investigate scarp morphology across the Les Saintes graben (Figure 4). A 10 m/pixel digital terrain model (DTM) and a backscatter map (Figure 3c) were gridded from shipboard multibeam bathymetric data acquired during the BATHYSAINTES cruise (see details in Leclerc et al., 2014, 2016). We used the 10 m/pixel data to provide continuous bathymetric coverage across the Les Saintes graben (Figure 2). During the 2013 ODEMAR cruise, AUV multibeam bathymetric data was acquired covering ~10 km² of the Roseau segment and gridded at 2 m/pixel (Figure 4). Complementing the AUV surveys, during the ODEMAR cruise, an ROV was used to collect multibeam bathymetric data closer to the seafloor along sections of the Roseau fault and bathymetric data was gridded at 50 and 10 cm/pixel (Figure 4) (see details in Escartín et al., 2016).

To improve the coverage of the existing bathymetry data, we conducted ROV and AUV surveys during the SUBSAINTES cruise, the latter at ~70 m above the seafloor using a Kongsberg Reson SMF EM2040 multibeam system. After processing, we gridded the SUBSAINTES AUV data at 1 m/pixel to produce very high-resolution DTMs covering an area of ~100 km^2 across multiple faults within the Les Saintes graben (Figure 4).

2.2. Three-Dimensional Terrain Models From Video Imagery

We collected video imagery at multiple locations along strike using the ROV's high-definition video camera during the SUBSAINTES cruise (ROV tracks are shown in Figure 4b). We processed this imagery to obtain three-dimensional terrain models at more than 40 locations across the Les Saintes graben (Figures 4b and S1). The imagery was corrected to improve the illumination, equalization, and color shift and we employed structure from motion techniques to create three-dimensional terrain models of each outcrop at ~1 cm resolution (e.g., Campos et al., 2015). We used texture-mapped models to facilitate visualization of features visible at the outcrop scale, while providing proper scaling for quantitative studies (Campos et al., 2015; Istenič et al., 2019, 2020). The data used in this study is a subset of 14 out the 41 three-dimensional models from the Roseau fault system (Figures 4b and S1; Table S2).

2.3. Seafloor Photomosaics

We used still-camera vertical images of the seafloor to complement the ROV video imagery. The vertical images from the ODEMAR cruise are in black-and-white and images from the SUBSAINTES cruise are in color. We processed imagery and ROV navigation to construct seafloor photomosaics for each of the dives using standard methods (e.g., Gracias et al., 2009) with a resolution of ~1 cm. These photomosaics provide visual ground truthing on the nature of the seafloor and various seafloor structures.

2.4. Rock Samples

In total, 201 rock samples were collected across the entire area of the Les Saintes graben using the ROV (Figure 4a). Around 65 samples from the Roseau fault reveal that the fault cuts across a range of extrusive volcanic and volcaniclastic deposits including andesitic lava, ferro-magnesian rich lavas, ignimbrites, and pyroclastics, which are often overlain by a thin drape of calcareous sediment that is generally less than 1 m thick (Table S3).

3. Observations of Seafloor Morphology

3.1. Regional Channel Network

The first order and largest-scale erosional features in the Les Saintes graben are the regional submarine drainage networks (Figure 2). The southwest flank of the Les Saintes reef plateau has an average slope of ~10° and a subdued topography with drainages that have up to 200 m relief from crest to thalweg. Fault scarps up to ~160 m high and dipping in the general uphill direction (i.e., to the northeast) interrupt the slope and pond sediments (Figure 2b). For example, channels that drain the southwest edge of the Les Saintes reef plateau predominantly trend to the southwest while channels draining the southern border of the reef plateau run in a southeasterly direction along the Roseau fault scarp so that sediments eroded from the southern edge of the reef plateau pond in the Roseau trough (Figure 2; Leclerc et al., 2016). The extent of ponded sediment is visible in the backscatter data where we interpret pale areas with low reflectivity to represent sedimentary cover (Figures 3c and 3d; Leclerc et al., 2016). Locally, channels that were probably initially connected to the reef plateau are now uplifted and cut from their initial source by uplift of the Roseau fault scarp (Figures 2 and 5; Leclerc et al., 2016). Consequently, the surface morphology of the northeast dipping Roseau fault scarp, presented below, is a product of local erosion processes but still influenced to some extent by the regional drainage network.
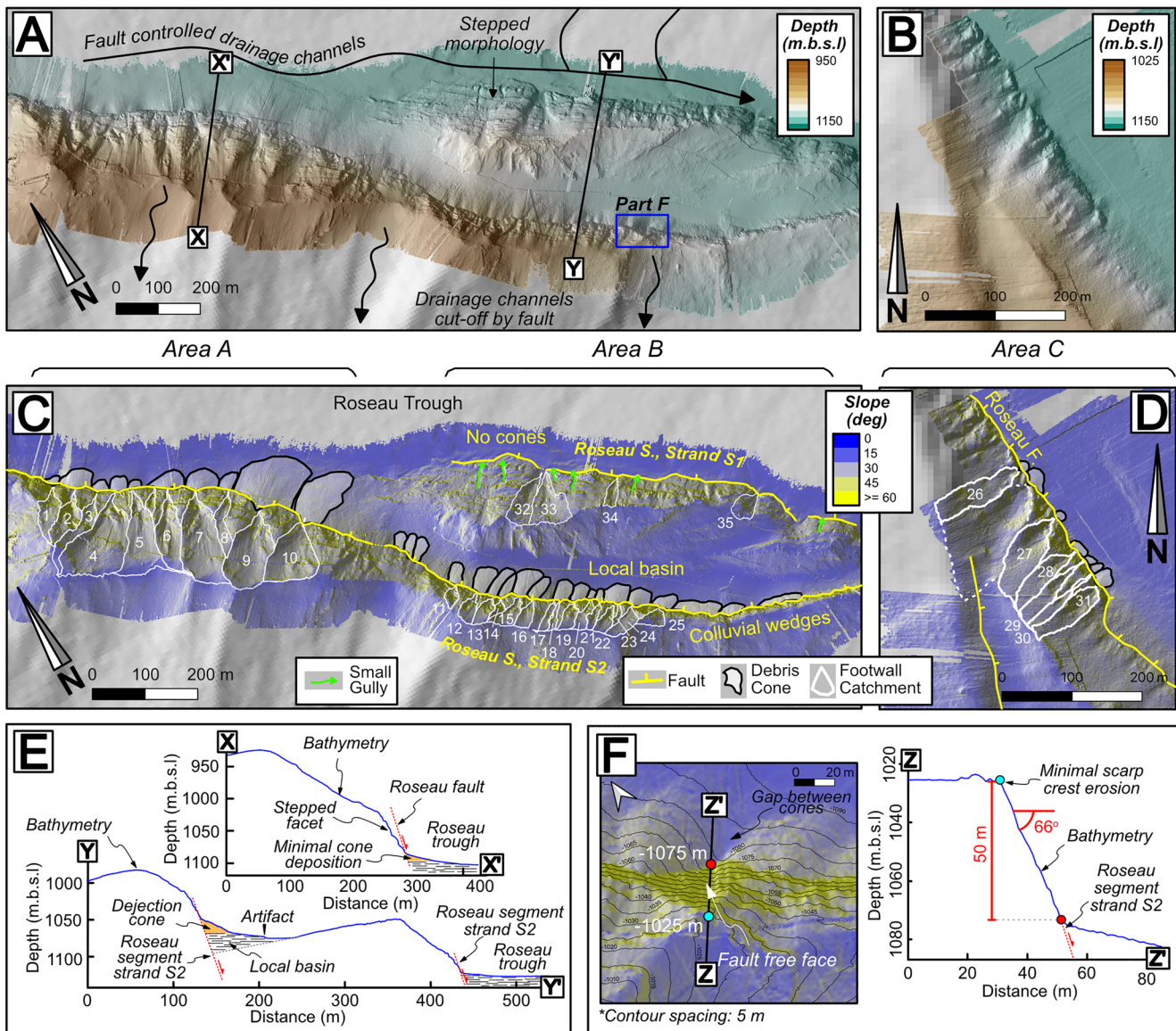
Figure 5. Footwall catchments and debris cones in areas A, B, and C of the Roseau segment. Figure locations are shown in Figure 3d. (a and b) Shaded relief maps derived from the 1 m/pixel digital terrain model (DTM). The black arrows show the approximate path of regional turbiditic drainage channels and demonstrate how uplift of the Roseau fault scarp has redirected regional drainage parallel to the fault. (c and d) Hillslope maps from the 1 m/pixel DTM showing the interpreted footwall catchment and debris cones. The numbers associated with the catchments refer to the data in Table S4. (e) Bathymetric section along the lines X–X′ and Y–Y′ (see part A for lines of section) showing the development of an uplifted local basin in the relay zone in area B (f) Enlarged hillslope map highlighting a 50 m high section of steep, relatively uneroded, fault free face along with bathymetric section Z–Z′ showing the steep scarp in cross section. The blue (top) and red (base) dots show corresponding points on the section and the map.

3.2. Surface Morphology of the Roseau Fault System

The Roseau fault scarp shows varying morphologies along strike (Figures 3, 5, and S2). For the northwestern part of the Roseau segment and the Canyon segment, the scarp is discontinuous and is only identifiable along the shoulders separating regional drainage channels, which postdate and, therefore, incise the scarp (Figure 2). In this area, the scarp reaches a maximum height of ~100 m and has slopes >40° in some places.

Along the southern border of the Roseau trough, scarp morphology becomes more pronounced as scarp height increases. The 1 m/pixel bathymetric data reveal that the Roseau segment is itself segmented and composed of three sub-segments separated from each other by relay zones with varying degrees of development (Figures 3 and 5). In particular, near the depocenter of the Roseau trough, a northern strand (herein

referred to as strand S1) and a southern strand (herein referred to as strand S2) overlap for 1.7 km and are spaced ∼300 m apart (Figures 3 and 5).

Footwall morphology of the Roseau segment varies from planar, high-slope (>60°) surfaces up to 50 m tall (Figure 5f), to sections with well-developed erosional footwall catchments, debris cones, and reduced high-slope surfaces in areas where scarp height approaches ∼100 m (Figure 5). In places, the scarp surface has a stepped morphology with individual steps occasionally >10 m in vertical height but are generally around 2–5 m in height. The stepped morphology is thought to reflect a succession of coseismic scarps, distributed faulting, and/or lithological layering (Leclerc et al., 2016), which, for the latter, could be enhanced by erosion from regional turbidity flows.

On the flanks of the Roseau volcano, which is cut by the Le Havre and Colibri segments, the seafloor appears rougher in shaded relief maps than on the other slopes off the Les Saintes islands. Accordingly, scarps associated with the Le Havre and Colibri segments are less well-defined and have relatively few identifiable erosional gullies, catchments, and debris cones. The Le Havre and Colibri segments are themselves segmented into a series of scarps with the exception of the northwestern end of the Le Havre segment, which is located in the Roseau trough and resembles the morphology of the Roseau segment with a series of erosional footwall catchments and debris cones (Figure S2).

In sediments on the continental slope, erosional valleys are often referred to as submarine canyons (e.g., Brothers et al., 2013; Mountjoy et al., 2018). Here, we refer to erosional valleys on the footwall of the scarp as footwall catchments. The term catchment is preferred because we interpret the most-developed catchments to be cirque-like amphitheaters that capture mass-wasted material from their flanks and funnel the eroded material off the scarp (see section 6.3). Catchments in the footwall of the Roseau fault are mapped along the Roseau, Le Havre, and the Colibri segments and generally occur where steep (>60°) surfaces are preserved at the base of the scarp (Figure S3). The footwall of strand S1 has a combination of well-developed footwall catchments along with small chutes and gullies, and the catchments drain directly into the Roseau trough (Figure 5). By contrast, well-developed footwall catchments present on the footwall of strand S2 of the Roseau segment drain into a small local basin of ∼ 0.2 km^2 within a relay zone (Figures 5c and 5e). The local basin is uplifted by 40–60 m relative to seafloor in the Roseau trough due to its location in the footwall of strand S1 (Figures 2b, 3, 5c and 5e).

3.3. Submeter-scale Observations

Various data sets characterize the submeter scale of the Roseau fault, including three-dimensional fault models, high-definition videos, photomosaics, and a 10 cm/pixel DTM that covers the surface area of three debris cones along the Roseau segment (Figures 6 and 7). The photomosaics provide semi-continuous images of the entire footwall surface covering three catchments along the Roseau segment (see ROV tracks in Figure 4a inset). At the top of the scarp, outside the catchment, the seafloor is largely covered by sediment with intermittent rubble (Figure 6c). The transition into the catchment is visible as a transition from mostly fine grained (drapes of silt to sand) to coarse grained (blocky rubble) sediment (respectively, pale and dark in Figures 6c and 6d). In the upper catchment, several small escarpments are visible both in the 0.5 m/pixel shaded relief map (Figures 6a and 6b) and in the photomosaics (Figure 6d). These small escarpments are located at the upper termination of sediment-filled channels that appear to funnel material out of the catchments and can be identified by pale streaks of sediment deposits oriented parallel to the thalweg and separated by abundant rubble deposited on top of layered bedrock (Figure 6f). At their maximum incision these shallow erosional channels are ∼1.5 m deep (Figure 6f). On the faces of the small escarpments in the upper catchment, brecciated deposits appear to have been draped over layered volcanic deposits providing evidence of active erosion in the upper catchment (Figure 6e). Lower down the slope of the catchment, the catchments narrow and the channels often lead into steep-sided erosional gullies near the catchment outlet (Figure 6g). Catchment outlets are separated by stepped facets (Figure 6b), which appear to be comprised of layers of in-situ breccia with minimal rubble cover (Figure 6h).

Along large sections of the Roseau fault, the lower section of the scarp is composed of a steep (60°–80°) plane, which at its base exhibits a relatively pale band of fresh bedrock up to ∼2.5 m high (Figure 7) that represents coseismic slip from the M$_w$ 6.3 2004 Les Saintes earthquake (Escartín et al., 2016). We interpret
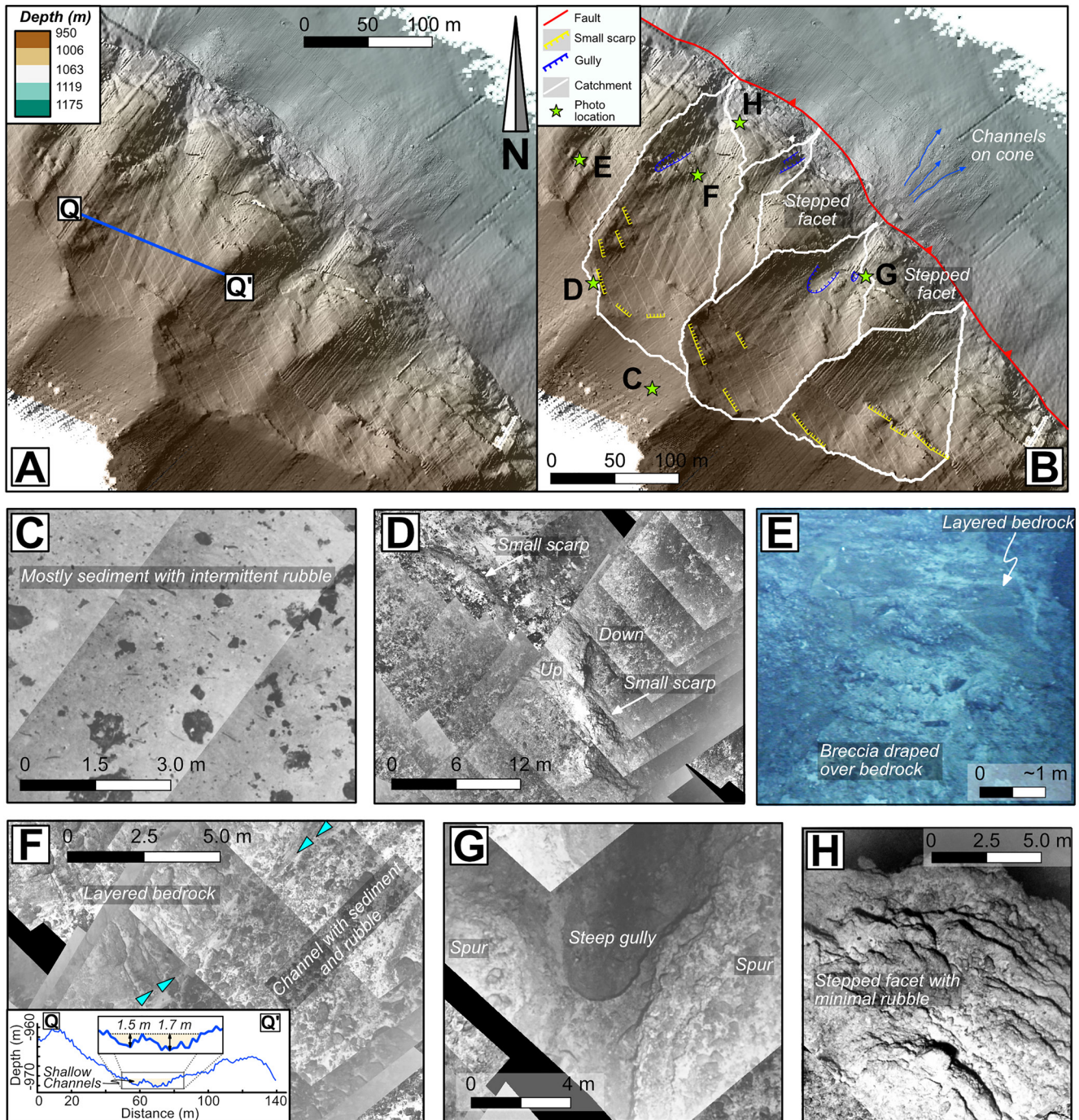
Figure 6. Erosional features throughout the footwall of the Roseau fault scarp. (a) Uninterpreted shaded relief map derived from the 50 and 10 cm/pixel digital terrain models. Part A is located in Figure 4a. (b) Interpreted map from part A showing the location of small escarpments and steep gullies along with the location of photos in parts C–H. (c) Photomosaic showing mostly sediment on the uneroded seafloor in the footwall. (d) A small escarpment in the upper catchment. (e) Screen shot from video imagery showing eroded breccia draped over layered bedrock. (f) A channel on the catchment surface which is filled with rubble and sediment and overlaps layered bedrock. The contact between deposited rubble and bedrock is highlighted by the blue arrows. Inset is bathymetric profile Q-Q′ (located in part A) showing the channels in cross section. (g) Steep-sided gullies in the lower catchment. The gully in the photomosaic is ~2–4 m deep. (h) Stepped bedrock with minimal sediment or rubble on a steep facet that separates catchment outlets. All photos are oriented with north toward the top.
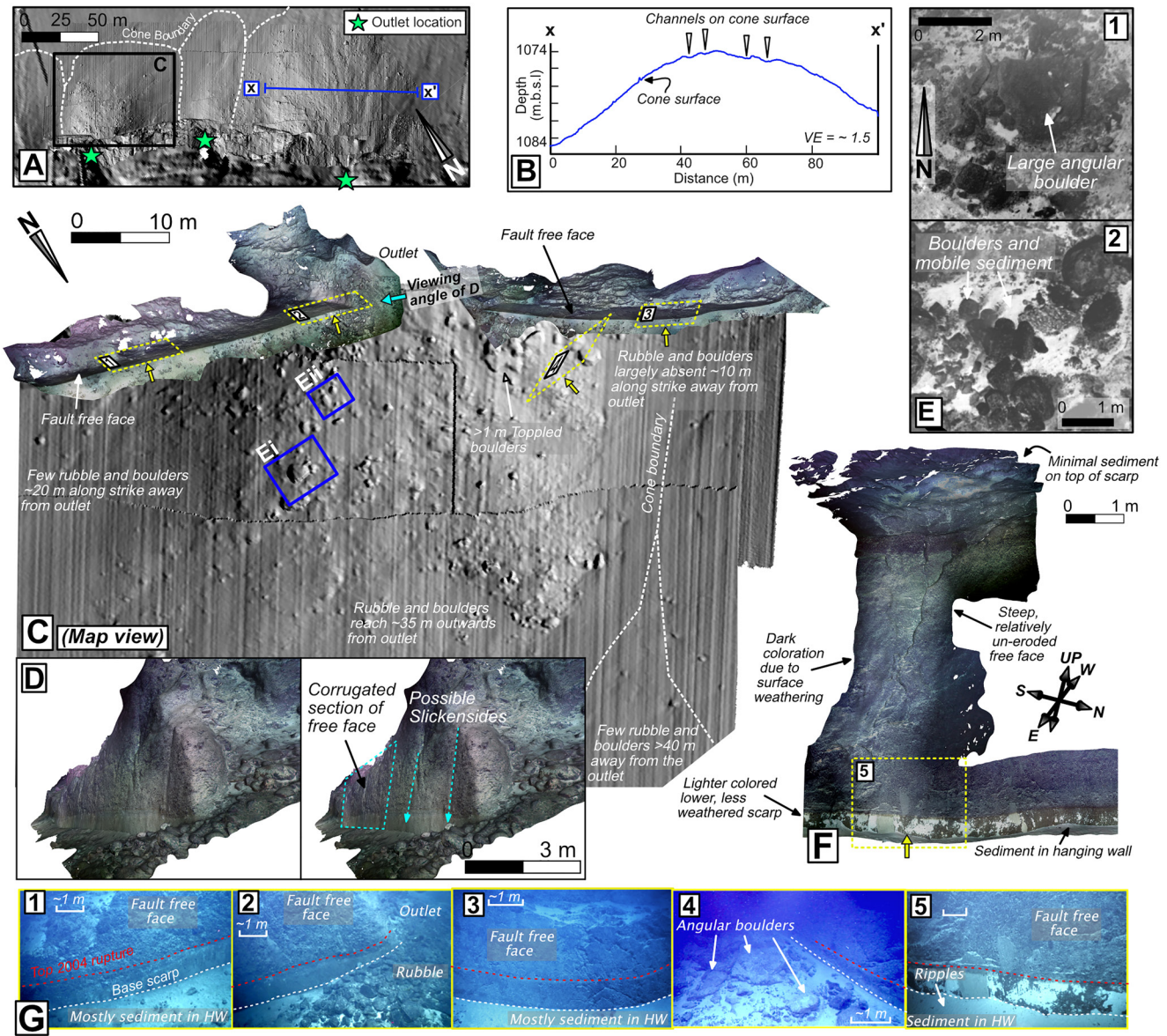
Figure 7. Submeter-scale morphology of depositional features associated with the Roseau fault scarp. (a) 10 cm/pixel digital terrain model (DTM) showing features of the cone surface. Part A is located in Figure 4a. (b) Bathymetric profile parallel to fault strike showing the dome shaped profile of the cones and channels on cone surface. VE = Vertical exaggeration. (c) Enlarged view of the 10 cm/pixel DTM overlain by video imagery-derived, three-dimensional outcrop models of the fault free face. The dashed yellow boxes are the location of the photos in G and the yellow arrows show photo directions. (d) Video imagery-derived, three-dimensional models with possible slickensides and corrugations on the fault free face. (e) Still imagery-derived photomosaics of boulders and rubble on the cone surface. (f) Video imagery-derived three-dimensional outcrop model of a ~10 m high uneroded section of steep scarp. The location of this model is shown in the inset of Figure 4a. (g) Screenshots from the video imagery showing various depositional features at the base of the fault slip plane and at catchment outlets. The white dashed line is the base of the scarp and the red dashed line is the top of recently exposed fault slip plane resulting from the Mw 6.3 Les Saintes earthquake (Escartín et al., 2016). HW = Hanging wall.

the full steep plane to represent the fault free face (e.g., Wallace, 1977). The free face is visible at a range of resolutions from the 1 m/pixel DTM (Figure 5a) to the submeter scale (Figure 7) and can reach up to 50 m tall (Figure 5f). In three-dimensional outcrop models and video footage, the free face is clearly visible as a smooth surface which is occasionally interrupted at catchments outlets and debris cones (Figures 7c and 7g). Striations, possibly slickensides, are visible on the free face in some of the three-dimensional models (Figure 7d) and above the free face, the scarp is eroded with a rougher and uneven surface. The base of the free face is hidden by sediments deposited on the hanging wall (Figure 7g). Occasional ripples are visible in the fine-grained sediments at the base of the scarp and indicate a transport direction parallel to
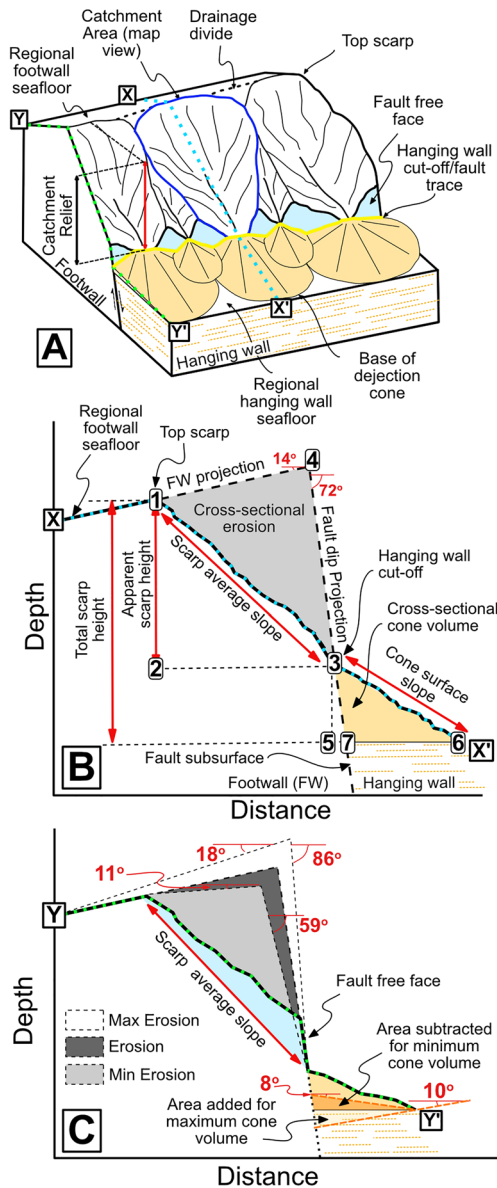
Figure 8. Parameters used to quantify the surface morphology of the Roseau fault. (a) Three-dimensional schematic view. (b) Schematic cross section along the line X–X′ showing a section through the scarp at a catchment outlet. The numbers in the boxes denote points referred to in the text to describe how we quantified scarp morphology, which is described in detail in the supplement. (c) Cross section view along the line Y–Y′ showing a transect through a section of scarp with exposed fault free face and the parameters used to quantify uncertainty in erosion measurements. The blue area outlines how scarp average slope may vary from the actual surface slope at a given point along the footwall.

the fault trace (Figures 7f and 7g). Where the free face is truncated by the outlet channels of the footwall catchments, rubble and angular boulders have been deposited on the hanging wall surface at the base of the scarp (Figure 7). The largest boulders are located near to catchment outlets and are well in excess of 1 m, with boulder size decreasing away from the catchment outlets (Figure 7c). The presence of such large boulders near the outlet suggest locally derived, gravity driven, mass-wasting deposits. The surfaces of the debris cones are also littered with large boulders surrounded by fine grained, mobile sediment that can be reworked by currents (Figures 7c, 7e, 7g). The 0.1 m/pixel DTM also shows channels on up to ∼5 m wide and ∼1 m deep incised on the surface of the largest debris cone (Figures 6b and 7b). In contrast, a three-dimensional model taken from a ∼10 m high, subvertical, uneroded section of the fault free face has no boulders or rubble deposited on top of sediments in the hanging wall (Figure 7f).

4. Quantification of Scarp Morphology and Erosion

The meter-scale morphological features of the Roseau fault described above clearly result from the interaction between tectonics, erosion by mass wasting, and sedimentation. To parameterize this interaction we performed various measurements using the methodology described below.

4.1. Methods

4.1.1. Scarp Mapping and Characterization

We extracted shaded relief, slope, and aspect maps from the 1 m/pixel DTM and used the maps to outline the extent and characterize the surface morphology of the Roseau fault system. An example of how we used the various maps to parameterize the scarp is included in Figure S4. We focused on the Roseau fault system for our quantitative analysis because it has the tallest exposed fault scarp (>150 m) within the Les Saintes graben. Additionally, constraints on the amount of erosion in the catchments and deposition in the debris cones of the Roseau segment allow a first-order estimate of the erosional volume balance between footwall and hanging wall.

To characterize empirical relationships between scarp morphology, erosion, and deposition during scarp development, we calculated scarp average slope and apparent scarp height from bathymetric profiles (Figure 8) for specific sections of the Canyon, Roseau, Le Havre, and Colibri segments of the Roseau fault system (yellow outlines in Figure 2). Scarp sections were selected based on availability of the 1 m/pixel DTM over most of the scarp and/or unambiguous identification of the base of the scarp identifiable in the 1 m/pixel DTM. The total distance measured along strike was ∼11.5 km. We also plotted scarp average slope, apparent scarp height, and cumulative scarp height (i.e., the sum of the height from strands S1 and S2 plus the height of talus in the hanging wall) along a continuous ∼7 km section of the Roseau segment (Figure 9, extracted from blue fault trace in Figure 2).

We measured apparent scarp height from the top of the scarp (point 1 in Figure 8b) to the hanging wall cut-off (point 3 in Figure 8b). We did not measure total scarp height from the top of the scarp to the base of hanging wall talus because the base of talus in the hanging wall (point 6 in Figure 8b) is often ambiguous
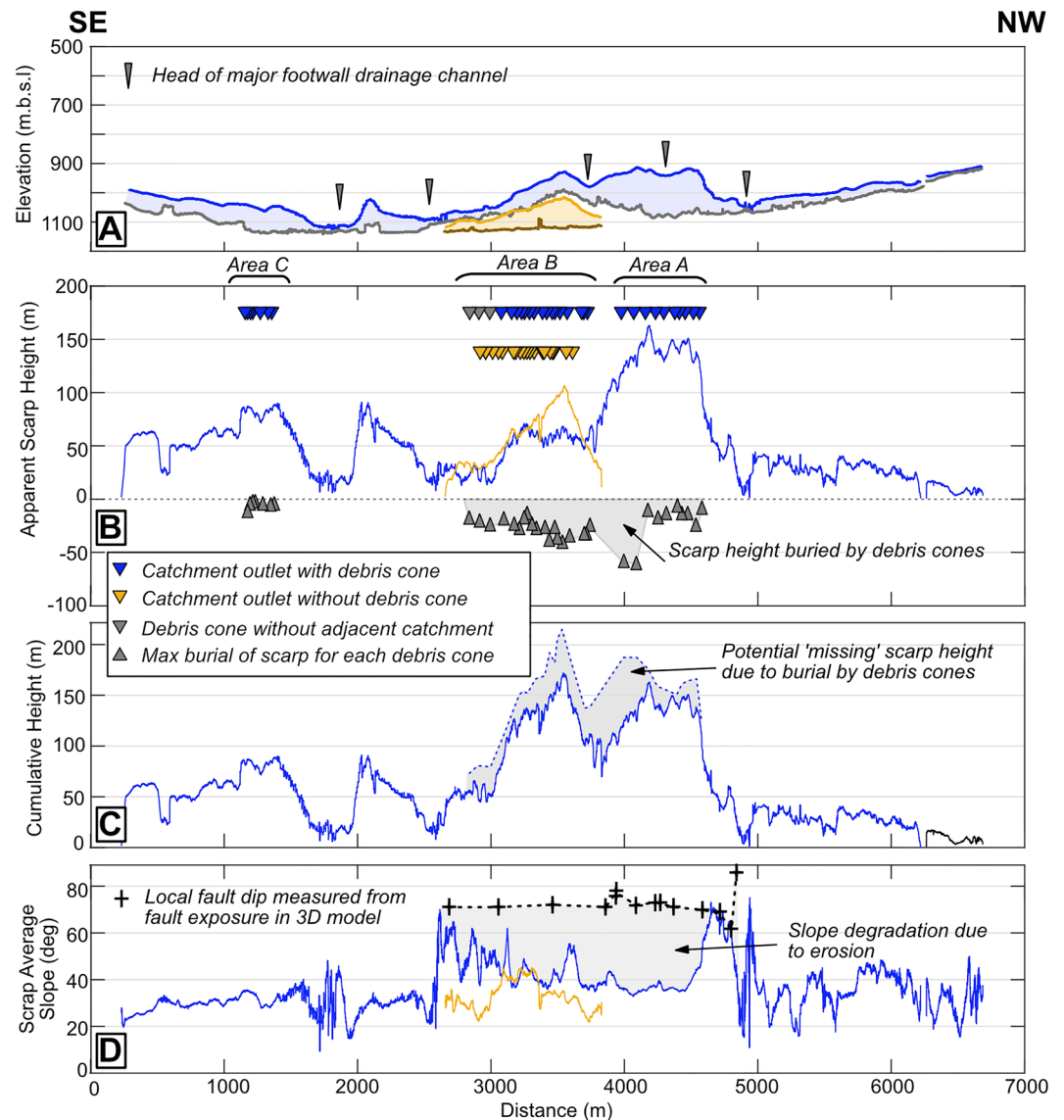
Figure 9. Along strike morphology of the Roseau segment based on blue fault trace in Figure 2. The blue lines correspond to the main Roseau segment (including strand S2) the yellow lines correspond to strand S1 where the faults overlap in the relay zone. (a) Bathymetry along strike. The blue and yellow lines represent bathymetry along the top of the scarp and the gray lines are bathymetry along the base of the scarp. The heads of major footwall drainage channels (thin triangles) correspond to local bathymetric lows along the top of the scarp. (b) Apparent scarp height along strike showing the location of footwall catchments and debris cones and the amount of scarp burial by debris cones. (c) Cumulative scarp height calculated by summing the heights of the two fault strands in area B. (d) Scarp average slope.

(Figure S5), whereas the hanging wall cut-off (point 3 in Figure 8b) is easier to identify in slope and/or shaded relief maps. The 1 m/pixel DTM does not provide continuous along-strike coverage for the entire footwall of the Roseau segment. Therefore, for our continuous along-strike plot, we supplemented the 1 m/pixel data with the 10 m/pixel data in areas of the footwall not covered by the 1 m/pixel data. We also measured the slope of the fault free face at 39 locations in 14 three-dimensional models using the software MESHLAB (Figure S1). The parameters used to quantify scarp morphology are shown schematically in Figure 8 and described in detail in the supporting information S1.
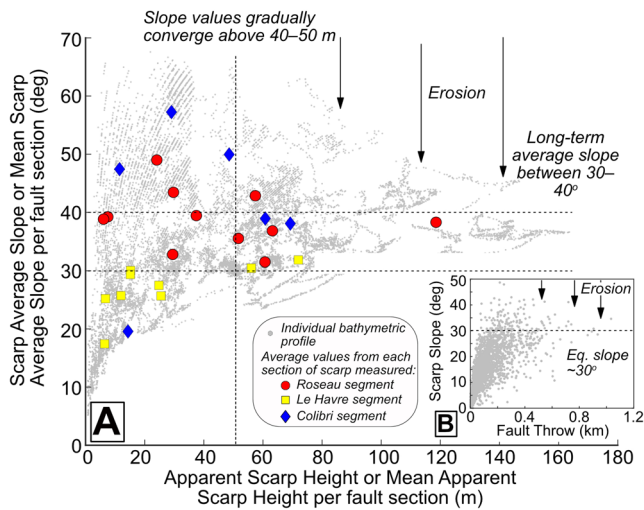
Figure 10. Morphological parameters for the Roseau fault. The data in A are based on the fault sections outlined in yellow in Figure 2. The gray dots are data points from each individual bathymetric profile whereas the colored shapes are the mean values for each section of fault measured. (a) Plot of scarp average slope vs. apparent scarp height for the Roseau fault. (b) Plot of fault throw versus scarp slope from the Chile Ridge taken from Howell et al. (2016).

4.1.2. Footwall Catchment and Debris-Cone Mapping

We performed volume-balancing calculations for 34 erosional footwall catchments and/or debris cones along the Roseau segment to compare volumes eroded from the footwall to volumes deposited in the hanging wall. Catchments in the footwall of the Roseau segment were extracted from the 1 m/pixel DTM with TopoToolbox (Schwanghart & Scherler, 2014). To quantify the volume eroded from footwall catchments (V_{FW}), we used bathymetric profiles spaced 1-m apart and oriented perpendicular to the direction of mean fault strike at the catchment outlet. We took the sum of eroded volumes from each profile along strike within the footprint of the catchment to be the catchment volume. The parameters used to quantify eroded volumes are included in Figure 8 and described in detail in the supplement.

We also calculated debris-cone volumes (V_{HW}) using bathymetric profiles spaced every meter and oriented normal to fault strike at the catchment outlet using the parameters shown in Figure 8. Due to variations in the dip of the seafloor in the hanging wall (i.e., toward the fault in places or away from the fault in others), debris-cone volumes were calculated assuming deposition on a flat surface similar to the calculations of Jayko (2005) (see discussion in Section 6.1.2). Variations in possible geometry of the seafloor in the hanging wall were incorporated into the uncertainty for the cone volumes (Figure 8c). Further details on the methodology and parameters employed to calculate cone volumes is provided in the supporting information S2.

4.2. Results

4.2.1. Scarp Slope, Height, and Erosion

We plotted the along-strike bathymetry, apparent scarp height, cumulative scarp height, and scarp average slope along strike for the Roseau segment (Figure 9) and we identified three areas (areas A, B, and C; Figure 3b) that have footwall catchments and/or debris cones. Along-strike bathymetry, apparent scarp height, and cumulative scarp height show considerable variability along strike and have maximum values located in areas A and B (Figure 9). Local lows in along-strike bathymetry and scarp height generally correspond to major drainage channels in the footwall (Figure 9a). Apparent scarp height ranges from <10 m to a maximum value of 164 m in area A (Figure 9b), but cumulative scarp height reaches a maximum value of ~170 m in the relay zone in area B (Figure 9c). Well-developed footwall catchments are generally only observed where scarp height is >50 m in maps derived from the 1 m/pixel or the 50 cm/pixel DTM (Figure 9c). Debris cones radiate from catchment outlets into the hanging wall in areas A, B and C. However, along strand S1 in area B, we note some large footwall catchments with no associated debris cones (Figure 5b). In area B, where apparent scarp height is ~20 m, a colluvial wedge is present in the hanging wall with several small channels or erosive ruts rather than well-developed catchments on the adjacent footwall (Figure S6). In the same area, an elongate fan is deposited in the hanging wall and protrudes out from the scarp much farther than the colluvial wedges to either side (Figure S6).

Scarp average slope for the Roseau segment exhibits significant variability along strike with values between 20°–40° and local highs of >70° located where scarp height is < 50 m at 2.5–3 km and 4.5–5 km along strike (Figure 9d). Footwall catchments and/or debris cones are generally mapped where scarp average slope is between 30° and 40° in areas A, B and C, although some cones toward the southeast end of area B correspond to higher slopes. The colluvial wedge occurs where scarp average slope increases above 60° in area B.

We also investigated the relationship between apparent scarp height and scarp average slope for selected sections of the Roseau, Le Havre, and Colibri segments of the Roseau fault. The plot of apparent scarp height versus scarp average slope shows that for apparent scarp heights below 40–50 m, scarp average slope can reach values approaching 70° (Figure 10a), which is similar to a ~72° mean dip of the fault free face

measured three-dimensional fault models (Figure S1c). The Roseau fault at depth is thought to dip 50° NE based on the distribution of aftershocks from the 2004 Les Saintes earthquake (Bazin et al., 2010). Therefore, we suggest that the Roseau fault must increase in dip as it approaches the surface as is commonly observed for normal fault systems (e.g., Jackson & McKenzie, 1983). As apparent scarp height increases above ∼40–50 m, the envelope defined by apparent scarp height and scarp average slope for each individual profile narrows (gray dots, Figure 10a). Additionally, above apparent scarp height of ∼60 m, the mean values of average scarp slope for each section of scarp measured (colored shapes, Figure 10a), all lie within the range of 30–40° (Figure 10a).

4.2.2. Footwall Catchments, Debris Cones, and Volume Balancing

Well-developed footwall catchments are generally found where the exposed scarp is higher than ∼50 m along sections of the Roseau, Le Havre, and Colibri segments of the Roseau fault system and along the Coche fault (Figure 2). Our analysis focused mainly on the Roseau segment because the 1 m/pixel DTM has the most complete coverage of the footwall scarp in this area. The catchments' long axes are oriented sub-perpendicular to fault strike, and the catchment outlines are generally elongated with width to length ratios that range from ∼0.15 to 0.60. Individual catchments are often separated between outlets by a steep fault free face and/or facets similar to a classical facet and spur morphology commonly documented in terrestrial catchments (e.g., Armijo et al., 1986; Bahrami, 2012; Wallace, 1978). Outlet spacings range from 50 to 100 m in area A and from 10 to 90 m in areas B and C. At its maximum extent in area A, headward erosion extends ∼200 m into the footwall but headward erosion only extends ∼10 m into the footwall for the steepest sections of the fault in area B (Figure 5).

Catchment area (a proxy for erosion) increases with catchment relief in a manner consistent with a power-law relationship of exponent of 2.3 (Figures 11a). For catchment areas below 4,000 m^2, mean catchment gradients range from ∼25° to 50° but as catchment area increases above 10,000 m^2 mean catchment gradients plot in the range of 30°–40° (Figures 11b). The range of 30°–40° is the same as the range of mean values above ∼60 m on the plot of apparent scarp height versus average scarp slope (Figure 10). Full details of catchment area, maximum catchment relief, and mean catchment gradients are included in Table S4.

Debris cones take the form of fan-shaped depositional features that radiate outwards from catchment outlets from the base of the scarp into the hanging wall. Average cone surface slopes are greatest in area B, where the mean of the average cone slopes is 29° and maximum slope values of 40° are recorded on two colluvial wedges. Cone surface slopes in areas A and C are lower with mean values of 18° and 20°, respectively (Figures 11c). The largest cones are mapped in area A, where cone volumes ranged from 1.3 x 10^3–2.1 × 10^5 m^3 and the ratio of footwall erosion to hanging wall deposition (V_{HW}/V_{FW}) is 0.18 (Figures 11c). In area B, debris cone volumes ranged from 1.8 × 10^3–3.7 × 10^4 m^3 and the cones in area B have a high V_{HW}/V_{FW} of 0.80 (Figures 11c). The cones in area C have the smallest volume, with a range in volume from 110 to 1,900 m^3 and a low V_{HW}/V_{FW} of 0.01 (Figures 11c). Full details of catchment and cone volumes are included in Table S5.

5. Discussion and Implications

The high-resolution data set from the Roseau fault has enabled us to characterize the morphology of the Roseau fault scarp at various scales and provides the framework to quantify relationships between scarp degradation and the evolution of scarp morphology with wider implications for erosion of the global seafloor.

5.1. Long-Term Rates of Landscape Evolution

5.1.1. Scarp Erosion Rate

The eroded volumes from the footwall of the Roseau segment (Figures 11c) enable us to estimate long-term erosion rates for the Roseau fault (E_{rf}) using the following equation:
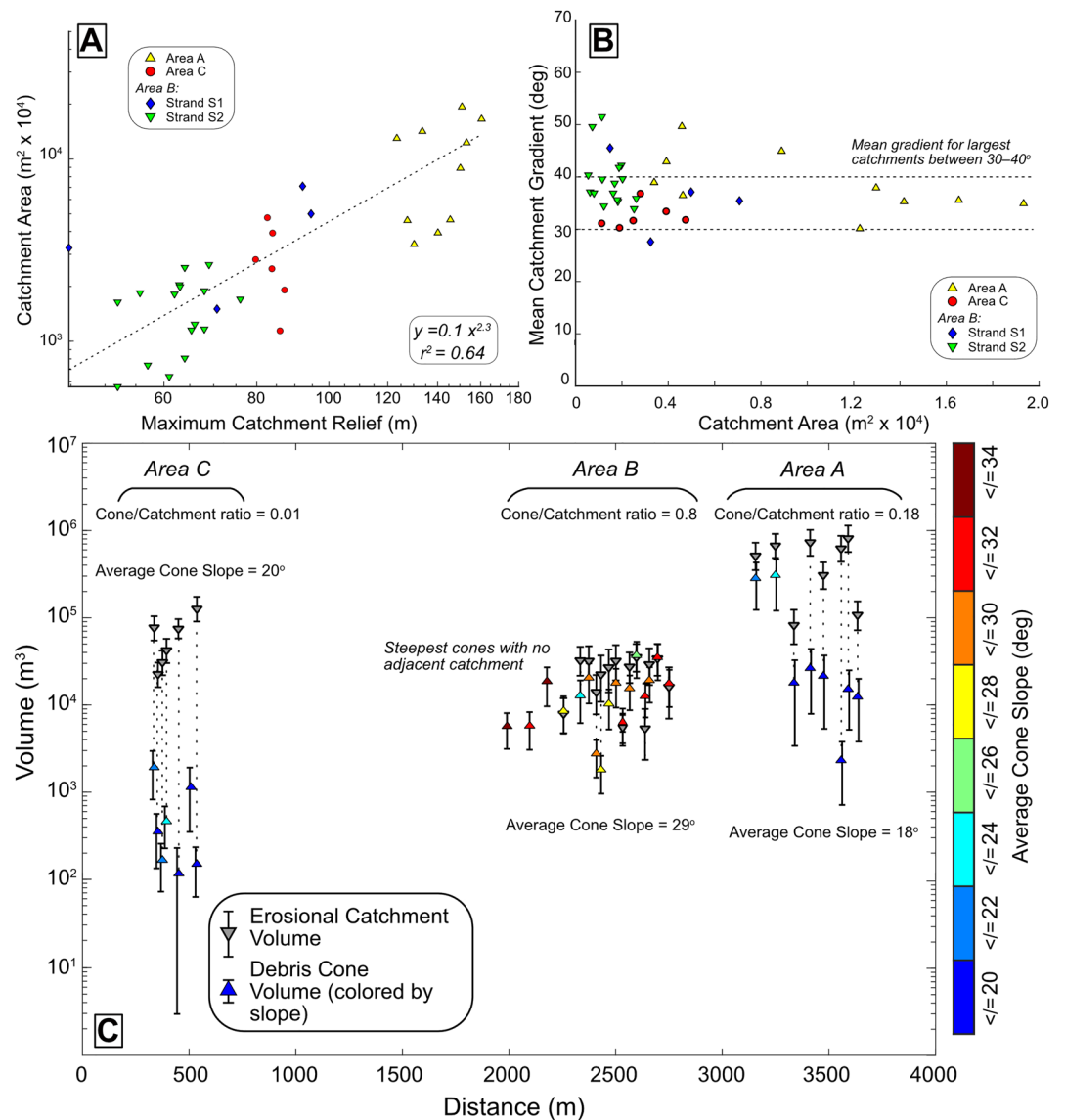
Figure 11. Catchment morphology and volume-balancing calculations. (a) Log-log plot of catchment area vs. catchment maximum relief. (b) Plot of mean catchment gradient vs. catchment area. (c) Volume comparison between footwall catchment erosion (downward pointing triangles) and hanging wall deposition in debris cones (upward pointing triangles). Debris cones are color coded based on the average slope of the cone surface. Note that the *y*-axis is logarithmic.

$$E_{rf} = \frac{\left(\frac{V_{fw}}{A_{fw}}\right)}{t_{rf}} \tag{1}$$

Equation 1 requires time constraints on the age of surface uplift related to the Roseau fault (t_{rf}). Seismic-reflection profiles imaging the relation between the Roseau volcano and the Roseau fault indicate that faulting postdates the emplacement of the volcano (Leclerc et al., 2016). There are no dates presently available for the youngest deposits from the Roseau volcano but terrestrial volcanism on the Les Saintes islands is thought to have occurred between 0.9 and 3.0 Ma (Zami et al., 2014). Using minimum $t_{rf} = 0.9$ Myr and maximum $t_{rf} = 3.0$ Myr, an average value for eroded volume in the highest section of the Roseau segment

in area A (V_{fw}) of $\sim$357,000 m^3, and an average corresponding catchment area (A_{fw}) of 8,700 m^2, we approximate a range of E_{rf} of 14–46 m Myr^{-1}.

For comparison, a minimum slip rate estimate for the Roseau fault based on the maximum age of terrestrial volcanism on Les Saintes of 3 Ma and 450 m of fault offset from seismic profiles is 0.15 mm yr^{-1} (or 150 m Myr^{-1}) (Leclerc et al., 2016). The minimum slip rate is between roughly three and 11 times larger than the minimum erosion rate. There are few estimates of erosion rates for submarine landscapes in the published literature, but erosion rates in submarine channels incised in a mixture of sediments and volcanic deposits on the flanks of the Canary Islands are 17–50 m Myr^{-1} (Mitchell et al., 2003). Average denudation rates for the period 4–24 Ma estimated from canyon cutting in volcanic bedrock with thin sedimentary cover at the Mid-Atlantic ridge are estimated at 10–20 m Myr^{-1} (Tucholke et al., 1997). Both of these ranges overlap with the erosion rate for the Roseau fault.

5.1.2. Earthquake-Induced Mass Wasting

While the data presented here provides little constraints on whether mass wasting primarily occurs in the coseismic, postseismic, or interseismic period, a comparison of seismicity data with further observations from three-dimensional outcrop models, photomosaics, and ROV video imagery indicates strong evidence for coseismic mass wasting with some minor postseismic erosion (Escartín et al., 2016, 2020). Elsewhere in the Lesser Antilles, evidence for coseismic triggered mass wasting of sediments has previously been identified from sediment cores and seismic data between Guadeloupe and Nevis (Beck et al., 2012).

Accordingly, we compare the erosion rate for the Roseau fault to earthquake-induced landslide erosion rates from subaerial settings. The range of 14–46 m Myr^{-1} for the Roseau fault overlaps with mean erosion rates from coseismic forcing in the Sierra Nevada, USA (18.2 m Myr^{-1}), Turkey (29.6 m Myr^{-1}), and central Japan (17.0–37.2 m Myr^{-1}), all of which are derived from regional landslide inventories and earthquake frequency-magnitude relationships (Keefer, 1994). Amongst other factors, the absence of water runoff and temperature fluctuations reduce the number and efficiency of denudational processes for the Roseau fault scarp compared to subaerial environments, yet it is noteworthy that the erosion rate from coseismic forcing at the submarine Roseau fault overlaps with terrestrial earthquake-induced landslide erosion rates across a range of tectonic, lithologic, and geographic settings. This suggests that earthquake-induced mass wasting may occur at comparable rates in the submarine and subaerial domains.

5.2. Erosion and Deposition at Both Regional and Local Scales

The regional drainage network around Les Saintes is an important large-scale erosion system that interacts with depositional features associated with local mass redistribution, such as debris cones. On the kilometer scale, pronounced fluctuations in height along the strike of the Roseau fault scarp (Figure 9) result from a two-way interaction between scarp growth and sedimentation, encompassing turbiditic sediment flows sourced from the Les Saintes reef plateau and pelagic or hemiplegic sediments, which bury parts of the scarp (Leclerc et al., 2016). The data in Figure 9b also demonstrate that exposed scarp height oscillates along strike on the decameter scale. This small-scale variation may partly result from another two-way interaction where the scarp grows during an earthquake but is simultaneously buried by the products of coseismic and/or postseismic mass-wasting (Escartín et al., 2016). Further evidence for simultaneous uplift and partial burial is provided in Figure 7g where the coseismically exposed rock toward the base of the scarp at the catchment outlet is buried by rubble clearly sourced from within the catchment.

Regional turbiditic erosion is also an important consideration when interpreting the results of the volume balancing. The absence of debris cones in the hanging wall of strand S1 of area B, coupled with the low $V_{\text{HW}}/V_{\text{FW}}$ in areas A and C (Figures 11c), probably results from partial or complete burial of the debris cones by sedimentation in the Roseau trough or possible removal of sediments via strong regional turbidity currents. Up to 300 m of sediment infill in the Roseau trough, identified in seismic profiles (Leclerc et al., 2016), is sourced from the Les Saintes reef plateau, the northern Savane trough, and the Roseau volcano (Figure 2). The hanging wall of area C is located in deepest part of the Roseau trough where sediment should be thickest and is also located $\sim$50 m downslope of the hanging wall of area A (Figure 9a). The difference in $V_{\text{HW}}/V_{\text{FW}}$ between area A (0.18) and area C (0.01) could reflect greater burial of the debris cones by sedimentation into the Roseau trough for area C compared to area A. In contrast, the debris cones along strand S2 in area

B are located in an isolated local basin where strand S1 forms a barrier and cuts off the hanging wall of strand S2 from external sediment sources within the relay zone (Figure 5). In this area, the V_{HW}/V_{FW} of 0.80 is higher because sources of sedimentation to bury the cones are limited to pelagic and hemipelagic sedimentation, or to sediment sourced from footwall of strand S2. Therefore, the volume of the debris cones in the hanging wall of strand S2 in area B may effectively embed the erosion signal from the footwall because there are fewer external sources of sediment to bury the cones.

Our debris-cone volumes assume deposition on a flat surface. The current seafloor geometry in the hanging wall along most of the Roseau segment is relatively flat but results from sedimentation into the Roseau trough or pelagic and hemipelagic sediment in the uplifted basin in the relay zone, both of which postdate uplift of the Roseau fault scarp. The seafloor in the footwall of strand S1 (effectively the initial seafloor in the hanging wall of strand S2) dips ∼10° toward the fault (Figure 5e), so the geometry of the seafloor at the onset of cone deposition depends on the rate of pelagic and hemipelagic sedimentation and how much pelagic sediment was present in the isolated basin at the onset of cone deposition. Unfortunately, we have no constraints on sedimentation rates and no high-resolution subsurface data to characterize the subsurface structure of the debris cones (e.g., chirp sonar). Regardless, possible variations in the seafloor are included in the uncertainty of the cone volumes and comparing either the maximum or minimum cone volumes in area B with the volumes of the associated catchments, still indicates that the cones in area B effectively record the erosion signal from the associated catchments. The variation in V_{HW}/V_{FW} between the individual catchments and cones probably results from interactions between the cones and burial of some parts of the cone flanks via eroded material from neighboring catchments.

5.3. Long-Term Scarp Evolution

Subaerial landscape erosion is driven to a large extent by water and ice runoff focused along valleys (e.g., Herman et al., 2015; Howard, 1994; Whipple & Tucker, 1999). On hillslopes, mass wasting processes play a more important role and are primarily driven by the gravitational force acting on the soil or rock itself (e.g., Densmore et al., 1997; Fernandes & Dietrich, 1997; Roering et al., 1999; Rosenbloom & Anderson, 1994). In uplifting extensional settings, these processes combine to alter the morphology of subaerial normal fault scarps where valleys carved in the footwall are separated by spurs and triangular facets, which may have a steeply dipping section of fault free face at their base as previously documented in the Basin and Range, USA (Wallace, 1977, 1978). Other classic examples of this morphology are documented in the Hellenic Arc, Greece (Armijo et al., 1991, 1992) and in southern Tibet (Armijo et al., 1986). In submarine environments, sediment gravity flows fed by mass wasting of unstable sediment deposits lead to the formation of submarine drainages on the continental slope that superficially resemble subaerial drainages despite differences in weathering and sediment transport processes (e.g., Brothers et al., 2013, Dobbs et al., 2019).

The Roseau segment scarp has a faceted spur morphology that is similar to classical examples of terrestrial normal fault scarps but is carved in submarine volcanic and volcaniclastic bedrock (Figures 5 and 6). Various contributing factors that trigger mass wasting in subaerial catchments or in submarine sediment dominated catchments on the continental slope are absent from the Roseau fault. Examples include: large volumes of unstable sediment deposits (Figure 6), physical weathering driven by temperature fluctuations (Eppes & Keanini, 2017), and production and transport of regolith on hillslopes (Densmore et al., 1998; Tucker et al., 2020). At mid-ocean ridges, fault scarps are thought to undergo gradual weathering via hydrothermal circulation in cracks and fissures and low-temperature alteration (Alt et al., 1986; Tucholke et al., 1997). The Roseau fault scarp surface shows both surface weathering and deposition of manganese coating, which indicates a degree of low-temperature alteration. However, we have no data on the extent to which possible low-temperature alteration weakens bedrock during scarp growth. Therefore, we speculate that erosion along the Roseau fault scarp should primarily result from the failure of more or less altered bedrock facilitated by coseismic shaking from earthquakes on either the Roseau fault or other regional faults, as observed along fault scarps at mid-ocean ridges (Allerton et al., 1995; Cannat et al., 2013; Goff & Tucholke, 1997; McAllister & Cann, 1996; Tucholke et al., 1997).
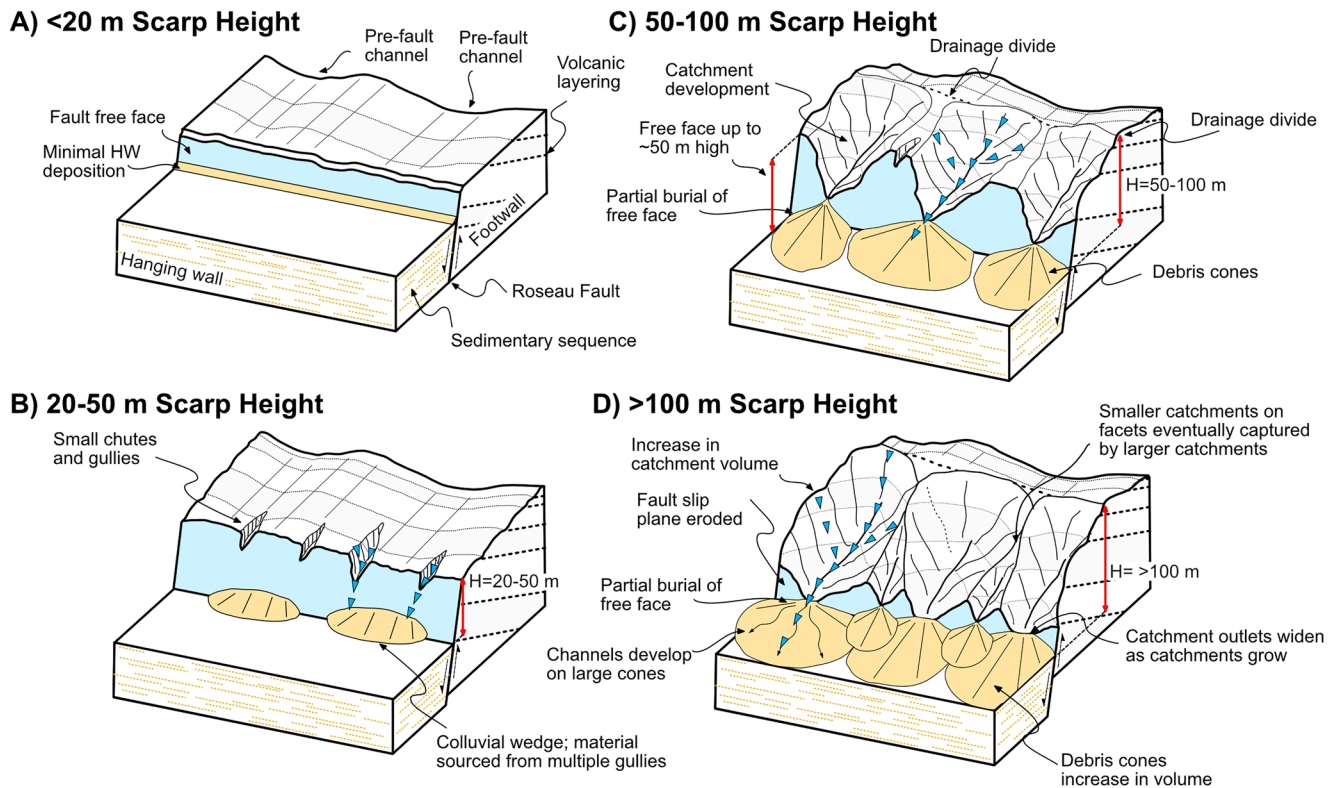
Figure 12. Schematic block models that outline the process-based model for submarine normal fault scarp evolution in volcanic basement lithologies. The fault free face is shaded light blue. Small blue arrows represent mass-wasting via rockfalls from the catchments into the debris cones. See text for full description of processes.

5.3.1. Scarp Evolution Model

The observations of seafloor morphology (Figures 6 and 7) along with the slope, height, and erosion data for the Roseau fault scarp (Figures 9–11) provide the framework for a process-based model for the evolution of active submarine normal fault scarps developing on basement or hard substrate (Figure 12). Over the timescale of scarp development, the model can be viewed as a continuous process where mass wasting maintains a critical scarp slope.

After the onset of surface uplift, submarine scarps develop as high-slope surfaces (the fault free face), which reflect the geometry of the fault plane in the shallow subsurface (Figure 12a). Relatively uneroded sections of the fault free face up to 50 m tall are observed along the Roseau (Figure 5f) and Colibri segments (Figure S2) but, in general, scarps become unstable and mass wasting begins when scarp height reaches 20–40 m (Figures 10 and 12b). We note that while we model the relationship between catchment maximum relief and catchment mean slope as a power-law fit (Figures 11a), the data also shows a good correlation using an exponential fit with an exponent of 0.02 (Figure S7). An exponential fit implies the existence of a characteristic relief, which using the exponent of 0.02 would be 50 m, and this is consistent with the maximum height of preserved free face of 50 m recorded in the study area. From the data presented here, it is unclear whether the threshold stability height of 20–40 m represents a time-threshold resulting from gradual weathering of the fault scarp due to low-temperature alteration or a stress threshold resulting from gravitational instability due to tectonic scarp growth. Regardless, at this early stage of scarp growth, deposition is not focused on the outlets of well-developed catchments but at several small chutes and gullies along strike (Figure 12b). The depositional product of the early erosion is a colluvial wedge with steep slopes that approach 40° in places (Figures 5c, 11c, and 12b).

The incipient steep gullies and head scars observed in the footwall catchments (Figure 6) are similar to larger-scale features recorded in slope-confined submarine canyons on the continental slope of northeastern

Australia (Puga-Bernabéu et al., 2011). Such features recorded in sediments are evidence of slope failure and upslope retrogressive erosion (Elliott et al., 2006; Green et al., 2007; Orange et al., 1997). In general, footwall catchments are associated with a section of critically steep scarp or fault free-face near the base of the scarp and catchments are less well developed in areas where there is a gradual decrease in slope from the footwall to the hanging wall (Figure S3). Accordingly, we suggest that above a certain height, that in our study area is ~20–40 m, gullies begin to erode into the free face via upslope retrogressive erosion (Figures 12b and S6). With further scarp growth above 40–50 m (such as in area B), the gullies begin to interact and form catchments that funnel mass-wasted material off the scarp and focus deposition into radial debris cones (Figure 12c). With scarp growth above ~100 m (such as in area A), catchments begin to expand and interact and the fault free face may become buried by hanging wall deposition while the slope of the footwall scarp evolves to between 30° and 40° (Figures 10a, 11b, and 12d).

Terrestrial catchments tend to follow Hack's Law where the length of a stream is related to the upstream drainage area by a power-law with exponent of 0.6 (Hack, 1957). Catchment erosion in the footwall of the Roseau fault is not driven by local stream incision but via mass wasting on the critically steep "hillslopes" of the fault scarp. Channels play a secondary role funneling material downslope which likely erodes the channel bed by plucking and abrasion. For the Roseau fault, we show that catchment area increases with catchment relief in a manner consistent with a power-law relationship of exponent of 2.3 (Figures 11a). This power-law relationship may point to a Hack's law-type relationship for submarine catchments where drainage area is a function of scarp height. However, further examples of submarine catchments from different lithological and geographic locations are needed to test the robustness of this relationship.

Rockfalls and possibly small rockslides are the most likely mechanisms for mass wasting along the Roseau fault scarp (Hungr et al., 2014; Varnes, 1978). Rockslides have previously been proposed as the key mechanism for mass wasting for submarine normal fault scarps in basaltic bedrock at the Mid-Atlantic ridge (Cannat et al., 2013). Evidence for rockfall is present in the abundant angular rubble and boulders on the surface of the debris cones and the footwall catchments (Figures 6 and 7). Turbidity flows are a key mass-wasting process associated with eroding sediments in submarine canyons on the continental slope (e.g., Hampton et al., 1996; Locat & Lee, 2002; Masson et al., 2006). For the Roseau fault, the small amount of fine sedimentary cover on the eroding footwall (Figures 6 and 7) could minimize the potential for entrainment of large volumes of fine sediment in turbidity currents. However, the small channels visible on the surface of the largest debris cone (Figure 7) appear to indicate some turbidity flows do initiate in the larger catchments. These turbidity flows likely entrain the thin layer of pelagic and hemipelagic sediments present on the catchment surface or fine sediments in the channels (Figure 6f). Additionally, we speculate that the elongate fan in area B (Figure S6) could result from mass wasting of a localized deposit of increased sediment thickness within the adjacent footwall.

The mechanics of submarine rockfall are similar to a subaerial environment except that grain disintegration is lessened by slower transport velocity and resulting lower energy grain impacts due to transport in water versus air (Mazzanti & De Blasio, 2013). Limited grain disintegration may explain the numerous angular boulders >1 m that are mapped on the cone surface (Figure 7c). Furthermore, headward erosion within the catchments has a maximum of ~200 m (Figure 5) and maximum catchment relief is 160 m (Table S4). The short potential transport distance and relatively low relief may also limit abrasion and grain disintegration during transport, which in turn will limit the production of fine-grained sediment within the catchments. Accordingly, we suggest the majority of fine sediment observed on the footwall and on the cone surfaces (Figures 6 and 7) is a mixture of pelagic and hemipelagic sediment, and mobile turbidite sediment sourced from the regional drainage network.

5.4. Implications for Submarine Landscape Evolution in Active Tectonics Settings

While the Roseau fault is situated in the Lesser Antilles volcanic arc (Figure 1), the underlying basement lithology and extensional tectonic setting make for a good approximation of normal faults at mid-ocean ridges. The mid-ocean ridge system is >65,000 km in length and plays a significant role in shaping topography for a large portion of the global seafloor. Previous studies of active submarine fault scarps at mid-ocean ridges have identified mass wasting as a significant erosional process (Allerton et al., 1995; Cannat et al., 2013; Goff & Tucholke, 1997; McAllister & Cann, 1996; Olive et al., 2019; Tucholke et al., 1997).

While there are few studies with high-resolution bathymetric data (resolutions <2 m) (Cannat et al., 2013), the morphology of the Roseau fault shares several characteristics with those described for active normal faults at mid-ocean ridges. For example, the gullies, catchments, and debris cones described in the footwall of the Roseau fault (Figures 5–7) are similar to features identified in normal fault scarps at various locations along the Mid-Atlantic ridge (Allerton et al., 1995; Goff & Tucholke, 1997; Tucholke et al., 1997). In terms of process, individual rockslides with surface areas of a similar magnitude to the debris cones identified for the Roseau fault (e.g., 100's of m^2) have been identified on the Mid-Atlantic ridge and are interpreted to form by non-cohesive granular flow (Cannat et al., 2013).

There are also subtle differences between the morphology of the Roseau fault scarp and scarp morphology described at mid-ocean ridges. For example, for mature normal faults with up to ~1,100 m of vertical displacement near the Kane fracture zone of the Mid-Atlantic ridge, debris cones have coalesced to produce a continuous wedge of sediment in the hanging wall that partially buries all but the upper portion of the footwall scarp (Allerton et al., 1995). Therefore, as submarine normal fault scarps mature beyond the current development of the Roseau fault scarp, a steady-state morphology may comprise a smaller section of incised footwall scarp, which is buried by a large wedge of mass-wasted sediment in the hanging wall.

Scarp average slopes for the Roseau fault tend toward 30°–40° for the tallest sections of the scarp or largest catchment areas (Figures 10a and 11b). The 30°–40° range is the same as the range reported for fault scarps North of the Kane Fracture Zone at the Mid-Atlantic ridge (Allerton et al., 1995), in basaltic deposits in the Krasnov area of the Mid-Atlantic ridge (Cannat et al., 2013), and in a global compilation of mid-ocean-ridge scarp slopes (Mitchell et al., 2000). Average slopes at the Chile Ridge for faults with the largest throw (>1 km) are slightly less than 30° (Figure 10b), but the distribution of average slope versus scarp height for the Chile Ridge (Howell et al., 2016) shows similarities to the same distribution for the Roseau fault (Figure 10). A similarity in slope/height profiles between faults with different displacements indicates that lithology may play an important role in the evolution of submarine fault scarp morphology (Cannat et al., 2013; Mitchell et al., 2000). Accordingly, the parameters identified here for the Roseau fault, such as the threshold height of 20–40 m for stability of subvertical fault slip surfaces, may vary in different tectonic and lithological settings (e.g., a similar threshold could be an order of magnitude larger in the basaltic seafloor of the Chile Ridge). Further work should seek to quantify these important relationships in order to constrain input parameters for models of submarine landscape evolution.

6. Conclusions

We employed automated deep-sea vehicles to acquire high-definition video imagery and high-resolution bathymetric data to document the decameter to submeter scale morphology along a pronounced surface scarp created by uplift of the Roseau normal fault in the Lesser Antilles volcanic arc. Evidence of active erosion, including channels, steep gullies, and small escarpments, is visible throughout the footwall. A subvertical fault free face is observed at the base of the scarp, which can reach up to 50 m tall and is interrupted in places by catchment outlets that feed coarse sediment to debris cones via rockfalls.

Using high-resolution bathymetric data, we undertook volume balancing to quantify the ratio of hanging wall deposition to footwall erosion (V_{HW}/V_{FW}). Where debris cones are being deposited into the Roseau trough, V_{HW}/V_{FW} is low (0.01–0.18) due to partial burial or removal of debris cones via regional sedimentation. By contrast, where external sediment supply is limited, we record V_{HW}/V_{FW} of 0.80 and debris cones effectively embed the erosion signal of mass-wasted material from the footwall. We utilized the eroded volumes from footwall catchments to calculate earthquake-induced landslide erosion rates for the Roseau fault of 14–46 m Myr^{-1}, which indicates that erosion via earthquake-induced mass wasting can occur at a similar rate in submarine setting to a variety of subaerial tectonic settings.

We used data on scarp average slope and apparent scarp height along the Roseau fault scarp as the framework for a process-based model for the evolution of submarine normal fault scarps in volcanic basement. Submarine normal faults scarps initially form as high-slope surfaces that mirror the dip of the fault in the shallow subsurface. With growth up to 20–40 m tall the scarp becomes unstable and retrogressive erosion via mass wasting gradually reduces scarp slopes to a long-term average slope of 30°–40° as scarp heights approaches 100 m.

Our survey of the Roseau fault scarp demonstrates that gravitationally driven mass-wasting is a significant process that controls scarp morphology during the growth of active submarine normal fault scarps in volcanic basement lithology. Ultimately, the data for the Roseau fault can potentially be used as inputs to develop quantitative long-term models of submarine landscape evolution based on normal fault scarp degradation. In order to develop quantitative models of submarine landscape evolution in basement lithologies, it is necessary to define a transfer function that links seismicity to ground shaking and mass wasting. Such complex relationships are the subject of ongoing study for mass wasting in terrestrial settings (Marc, Hovius, Meunier, Gorum, 2016) and further work should link these processes to submarine normal faults to develop submarine landscape evolution models.

Data Availability Statement

We are indebted to the crew, officers, and engineers during the ODEMAR (2013) and SUBSAINTES (2017) cruises, whose efficient work and dedication allowed us to acquire the data used in this study, and to the contributions of the science parties on both cruises. Data is from fieldwork conducted during the ODEMAR 2013 cruise (PIs J. Escartín & M. Andreani, https://doi.org/10.17600/13030070), and the SUBSAINTES 2017 cruise (PI J. Escartín, co-PIs: N. Feuillet & A. Le Friant, https://doi.org/10.17600/17001000).

References

Allerton, S., Murton, B. J., Searle, R. C., & Jones, M. (1995). Extensional faulting and segmentation of the Mid-Atlantic Ridge north of the Kane Fracture Zone (24° 00′ N to 24° 40′ N). *Marine Geophysical Research*, *17*(1), 37–61. https://doi.org/10.1007/BF01268050

Alt, J. C., Honnorez, J., Laverne, C., & Emmermann, R. (1986). Hydrothermal alteration of a 1 km section through the upper oceanic crust, Deep Sea Drilling Project Hole 504B: Mineralogy, chemistry and evolution of seawater-basalt interactions. *Journal of Geophysical Research*, *91*(B10), 10309–10335. https://doi.org/10.1029/jb091ib10p10309

Armijo, R., Lyon-Caen, H., & Papanastassiou, D. (1991). A possible normal-fault rupture for the 464 BC Sparta earthquake. *Nature*, *351*(6322), 137–139. https://doi.org/10.1038/351137a0

Armijo, R., Lyon-Caen, H., & Papanastassiou, D. (1992). East-west extension and Holocene normal-fault scarps in the Hellenic arc. *Geology*, *20*(6), 491–494. https://doi.org/10.1130/0091-7613(1992)020<0491:EWEAHN>2.3.CO;2

Armijo, R., Pondard, N., Meyer, B., Ucarkus, G., De Lépinay, B. M., Malavieille, J., et al. (2005). Submarine fault scarps in the Sea of Marmara pull-apart (North Anatolian Fault): Implications for seismic hazard in Istanbul. *Geochemistry, Geophysics, Geosystems*, *6*, Q06009. https://doi.org/10.1029/2004GC000896

Armijo, R., Tapponnier, P., Mercier, J. L., & Han, T.-L. (1986). Quaternary extension in southern Tibet: Field observations and tectonic implications. *Journal of Geophysical Research*, *91*(B14), 13803. https://doi.org/10.1029/jb091ib14p13803

Avouac, J.-P. (1993). Analysis of scarp profiles: Evaluation of errors in morphologic dating. *Journal of Geophysical Research*, *98*(B4), 6745–6754. https://doi.org/10.1029/92jb01962

Bahrami, S. (2012). Morphotectonic evolution of triangular facets and wine-glass valleys in the Noakoh anticline, Zagros, Iran: Implications for active tectonics. *Geomorphology*, *159–160*, 37–49. https://doi.org/10.1016/j.geomorph.2012.03.003

Bazin, S., Feuillet, N., Duclos, C., Crawford, W., Nercession, A., Bengoubou-Valérius, M., et al. (2010). The 2004-2005 Les Saintes (French West Indies) seismic aftershock sequence observed with ocean bottom seismometers. *Tectonophysics*, *489*(1–4), 91–103. https://doi.org/10.1016/j.tecto.2010.04.005

Beck, C., Reyss, J.-L., Leclerc, F., Moreno, E., Feuillet, N., Barrier, L., et al. (2012). Identification of deep subaqueous co-seismic scarps through specific coeval sedimentation in Lesser Antilles: Implication for seismic hazard. *Natural Hazards and Earth System Sciences*, *12*(5), 1755–1767. https://doi.org/10.5194/nhess-12-1755-2012

Bilal, A., McClay, K., & Scarselli, N. (2018). *Fault-scarp degradation in the central Exmouth plateau*. North West Shelf, Australia: Geological Society, London, Special Publications. SP476.11 https://doi.org/10.1144/sp476.11

Brothers, D. S., ten Brink, U. S., Andrews, B. D., Chaytor, J. D., & Twichell, D. C. (2013). Geomorphic process fingerprints in submarine canyons. *Marine Geology*, *337*, 53–66. https://doi.org/10.1016/j.margeo.2013.01.005

Campos, R., Garcia, R., Alliez, P., & Yvinec, M. (2015). A surface reconstruction method for in-detail underwater 3D optical mapping. *The International Journal of Robotics Research*, *34*(1), 64–89. https://doi.org/10.1177/0278364914544531

Cannat, M., Mangeney, A., Ondréas, H., Fouquet, Y., & Normand, A. (2013). High-resolution bathymetry reveals contrasting landslide activity shaping the walls of the Mid-Atlantic Ridge axial valley. *Geochemistry, Geophysics, Geosystems*, *14*, 996–1011. https://doi.org/10.1002/ggge.20056

Coleman, J. M., & Prior, D. B. (1988). Mass wasting on continental margins. *Annual Review of Earth and Planetary Sciences*, *16*, 101–119.1929. https://doi.org/10.1146/annurev.ea.16.050188.000533

Contreras-Reyes, E., Völker, D., Bialas, J., Moscoso, E., & Grevemeyer, I. (2016). Reloca Slide: an ~24 km^3 submarine mass-wasting event in response to over-steepening and failure of the central Chilean continental slope. *Terra Nova*, *28*(4), 257–264. https://doi.org/10.1111/ter.12216

Crosby, B. T., & Whipple, K. X. (2006). Knickpoint initiation and distribution within fluvial networks: 236 waterfalls in the Waipaoa River, North Island, New Zealand. *Geomorphology*, *82*(1–2), 16–38. https://doi.org/10.1016/j.geomorph.2005.08.023

DeMets, C., Jansma, P. E., Mattioli, G. S., Dixon, T. H., Farina, F., Bilham, R., et al. (2000). GPS geodetic constraints on Caribbean-North America Plate Motion. *Geophysical Research Letters*, *27*(3), 437–440. https://doi.org/10.1029/1999gl005436

Deng, J., & Sykes, L. R. (1995). Determination of Euler pole for contemporary relative motion of Caribbean and North American plates using slip vectors of interplate earthquakes. *Tectonics*, *14*(1), 39–53. https://doi.org/10.1029/94TC02547

Densmore, A. L., Anderson, R. S., McAdoo, B. G., & Ellis, M. A. (1997). Hillslope evolution by bedrock landslides. *Science*, *275*(5298), 369–372. https://doi.org/10.1126/science.275.5298.369

Densmore, A. L., Ellis, M. A., & Anderson, R. S. (1998). Landsliding and the evolution of normal-fault-bounded mountains. *Journal of Geophysical Research*, *103*(B7), 15203–15219. https://doi.org/10.1029/98jb00510

Deplus, C., & Feuillet, N., (2010). *BATHYSAINTES cruise, RV Pourquoi Pas?* https://doi.org/10.17600/10030020

Dixon, T. H., Farina, F., DeMets, C., Jansma, P., Mann, P., & Calais, E. (1998). Relative motion between the Caribbean and North American plates and related boundary zone deformation from a decade of GPS observations. *Journal of Geophysical Research*, *103*(B7), 15157–15182. https://doi.org/10.1029/97jb03575

Dobbs, S. C., McHargue, T., Malkowski, M. A., Gooley, J. T., Jaikla, C., White, C. J., & Hilley, G. E. (2019). Are submarine and subaerial drainages morphologically distinct? *Geology*, *47*(11), 1093–1097. https://doi.org/10.1130/g46329.1

Elliott, G. M., Shannon, P. M., Haughton, P. D. W., Praeg, D., & O'Reilly, B. (2006). Mid- to Late Cenozoic canyon development on the eastern margin of the Rockall Trough, offshore Ireland. *Marine Geology*, *229*(3–4), 113–132. https://doi.org/10.1016/j.margeo.2006.03.008

Elliott, G. M., Wilson, P., Jackson, C. A.-L., Gawthorpe, R. L., Michelsen, L., & Sharp, I. R. (2012). The linkage between fault throw and footwall scarp erosion patterns: An example from the Bremstein Fault Complex, offshore Mid-Norway. *Basin Research*, *24*(2), 180–197. https://doi.org/10.1111/j.1365-2117.2011.00524.x

Ellis, M. A., Densmore, A. L., & Anderson, R. S. (1999). Development of mountainous topography in the Basin Ranges, USA. *Basin Research*, *11*(1), 21–41. https://doi.org/10.1046/j.1365-2117.1999.00087.x

Eppes, M.-C., & Keanini, R. (2017). Mechanical weathering and rock erosion by climate-dependent subcritical cracking. *Journal of Geophysical Research: Reviews of Geophysics*, *55*, 470–508. https://doi.org/10.1002/2017RG000557

Escartin, J., & Andreani, M. (2013). *ODEMAR cruise, RV Pourquoi Pas?* https://doi.org/10.17600/13030070

Escartin, J., Billant, J., Leclerc, F., Olive, J.-A., Istenič, K., Gracias, N., et al. (2020). *Connecting seismicity, gravity-driven erosion and deposition at submarine normal faults: Insights from mapping of the 2004 Mw 6 . 3 Les Saintes earthquake rupture (French Antilles)*. Online: 22nd EGU General Assembly.

Escartín, J., Leclerc, F., Olive, J.-A., Mevel, C., Cannat, M., Petersen, S., et al. (2016). First direct observation of coseismic slip and seafloor rupture along a submarine normal fault and implications for fault slip history. *Earth and Planetary Science Letters*, *450*, 96–107. https://doi.org/10.1016/j.epsl.2016.06.024

Escartín, J., Le Friant, A., & Feuillet, N. (2017). *Subsaintes cruise report, n/o l'atalante-rov victor-auv asterx. Fr. Oceanogr. Cruises*. https://doi.org/10.17600/17001000

Fernandes, N. F., & Dietrich, W. E. (1997). Hillslope evolution by diffusive processes: The timescale for equilibrium adjustments. *Water Resources Research*, *33*(6), 1307–1318. https://doi.org/10.1029/97wr00534

Feuillet, N., Beauducel, F., Jacques, E., Tapponnier, P., Delouis, B., Bazin, S., et al. (2011). The Mw = 6.3, November 21, 2004, les Saintes earthquake (Guadeloupe): Tectonic setting, slip model and static stress changes. *Journal of Geophysical Research*, *116*(10). https://doi.org/10.1029/2011JB008310

Feuillet, N., Leclerc, F., Tapponnier, P., Beauducel, F., Boudon, G., Le Friant, A., et al. (2010). Active faulting induced by slip partitioning in montserrat and link with volcanic activity: New insights from the 2009 GWADASEIS marine cruise data. *Geophysical Research Letters*, *37*, 1–6. https://doi.org/10.1029/2010GL042556

Feuillet, N., Manighetti, I., Tapponnier, P., & Jacques, E. (2002). Arc parallel extension and localization of volcanic complexes in Guadeloupe, Lesser Antilles. *Journal of Geophysical Research*, *107*(B12). 2331. https://doi.org/10.1029/2001jb000308

Goff, J. A., & Tucholke, B. E. (1997). Multiscale spectral analysis of bathymetry on the flank of the Mid-Atlantic Ridge: Modification of the seafloor by mass wasting and sedimentation. *Journal of Geophysical Research*, *102*. https://doi.org/10.1029/97jb00723

Gracias, N., Mahoor, M., Negahdaripour, S., & Gleason, A. (2009). Fast image blending using watersheds and graph cuts. *Image and Vision Computing*, *27*(5), 597–607. https://doi.org/10.1016/j.imavis.2008.04.014

Green, A. N., Goff, J. A., & Uken, R. (2007). Geomorphological evidence for upslope canyon-forming processes on the northern KwaZulu-Natal shelf, SW Indian Ocean, South Africa. *Geo-Marine Letters*, *27*(6), 399–409. https://doi.org/10.1007/s00367-007-0082-2

Hack, J. T. (1957). Studies of Longitudinal Stream Profiles in Virginia and Maryland, (294). US Government Printing Office.

Hampton, M. A., Lee, H. J., & Locat, J. (1996). Submarine landslides. *Journal of Geophysical Research*, *34*(1), 33–59. https://doi.org/10.1029/95RG03287

Henstra, G. A., Grundvåg, S.-A., Johannessen, E. P., Kristensen, T. B., Midtkandal, I., Nystuen, J. P., et al. (2016). Depositional processes and stratigraphic architecture within a coarse-grained rift-margin turbidite system: The Wollaston Forland Group, east Greenland. *Marine and Petroleum Geology*, *76*, 187–209. https://doi.org/10.1016/j.marpetgeo.2016.05.018

Herman, F., Beyssac, O., Brughelli, M., Lane, S. N., Leprince, S., Adatte, T., et al. (2015). Erosion by an Alpine glacier. *Science*, *350*(6257), 193–195. https://doi.org/10.1126/science.aab2386

Hilley, G. E., Sare, R. M., Aron, F., Baden, C. W., Caress, D. W., Castillo, C. M., et al. (2020). Coexisting seismic behavior of transform faults revealed by high-resolution bathymetry. *Geology*. https://doi.org/10.1130/g46663.1

Howard, A. D. (1994). A detachment-limited model of drainage basin evolution. *Water Resources Research*, *30*(7), 2261–2285. https://doi.org/10.1029/94WR00757

Howell, S. M., Ito, G., Behn, M. D., Martinez, F., Olive, J.-A., & Escartín, J. (2016). Magmatic and tectonic extension at the Chile Ridge: Evidence for mantle controls on ridge segmentation. *Geochemistry, Geophysics, Geosystems*, *17*, 2354–2373. https://doi.org/10.1002/2016GC006380

Hungr, O., Leroueil, S., & Picarelli, L. (2014). The Varnes classification of landslide types, an update. *Landslides*, *11*(2), 167–194. https://doi.org/10.1007/s10346-013-0436-y

Istenič, K., Gracias, N., Arnaubec, A., Escartín, J., & Garcia, R. (2019). Scale accuracy evaluation of image-based 3D reconstruction strategies using laser photogrammetry. *Remote Sensing*, *11*(18). https://doi.org/10.3390/rs11182093

Istenič, K., Gracias, N., Arnaubec, A., Escartín, J., & Garcia, R. (2020). Automatic scale estimation of structure from motion based 3D models using laser scalers in underwater scenarios. *ISPRS Journal of Photogrammetry and Remote Sensing*, *159*, 13–25. https://doi.org/10.1016/j.isprsjprs.2019.10.007

Jackson, J., & McKenzie, D. (1983). The geometrical evolution of normal fault systems. *Journal of Structural Geology*, *5*(5), 471–482. https://doi.org/10.1016/0191-8141(83)90053-6

Jackson, J. A., & White, N. J. (1989). Normal faulting in the upper continental crust: observations from regions of active extension. *Journal of Structural Geology*, *11*(1–2), 15–36. https://doi.org/10.1016/0191-8141(89)90033-3

Jayko, A. S. (2005). Late Quaternary denudation, Death and Panamint valleys, eastern California. *Earth-Science Reviews*, *73*(1–4), 271–289. https://doi.org/10.1016/j.earscirev.2005.04.009

Jordan, T. H. (1975). The present-day motions of the Caribbean Plate. *Journal of Geophysical Research*, *80*(32), 4433–4439. https://doi.org/10.1029/jb080i032p04433

Katz, O., Reuven, E., & Aharonov, E. (2015). Submarine landslides and fault scarps along the eastern Mediterranean Israeli continental-slope. *Marine Geology*, *369*, 100–115. https://doi.org/10.1016/j.margeo.2015.08.006

Keefer, D. K. (1994). The importance of earthquake-induced landslides to long-term slope erosion and slope-failure hazards in seismically active regions. *Geomorphology and Natural Hazards*. *10*. https://doi.org/10.1016/b978-0-444-82012-9.50022-0

Kirby, E., & Whipple, K. X. (2012). Expression of active tectonics in erosional landscapes. *Journal of Structural Geology*, *44*, 54–75. https://doi.org/10.1016/j.jsg.2012.07.009

Leclerc, F., Feuillet, N., Cabioch, G., Deplus, C., Lebrun, J. F., Bazin, S., et al. (2014). The Holocene drowned reef of Les Saintes plateau as witness of a long-term tectonic subsidence along the Lesser Antilles volcanic arc in Guadeloupe. *Marine Geology*, *355*, 115–135. https://doi.org/10.1016/j.margeo.2014.05.017

Leclerc, F., Feuillet, N., & Deplus, C. (2016). Interactions between active faulting, volcanism, and sedimentary processes at an island arc: Insights from Les Saintes channel, Lesser Antilles arc. *Geochemistry, Geophysics, Geosystems*. *17*, 2781–2802. https://doi.org/10.1002/2016GC006337

Leeder, M. R., & Gawthorpe, R. L. (1987). Sedimentary models for extensional tilt-block/half-graben basins. *Geological Society Special Publication*, *28*, 139–152. https://doi.org/10.1144/GSL.SP.1987.028.01.11

Le Friant, A., Heinrich, P., & Boudon, G. (2008). Field survey and numerical simulation of the 21 November 2004 tsunami at Les Saintes (Lesser Antilles). *Geophysical Research Letters*, *35*, L12308. https://doi.org/10.1029/2008GL034051

Leynaud, D., Mienert, J., & Vanneste, M. (2009). Submarine mass movements on glaciated and non-glaciated European continental margins: A review of triggering mechanisms and preconditions to failure. *Marine and Petroleum Geology*, *26*(5), 618–632. https://doi.org/10.1016/j.marpetgeo.2008.02.008

Locat, J., & Lee, H. J. (2002). Submarine landslides: Advances and challenges. *Canadian Geotechnical Journal*, *39*(1), 193–212. https://doi.org/10.1139/t01-089

López, A. M., Stein, S., Dixon, T., Sella, G., Calais, E., Jansma, P., et al. (2006). Is there a northern Lesser Antilles forearc block? *Geophysical Research Letters*, *33*, L07313 . https://doi.org/10.1029/2005gl025293

Marc, O., Hovius, N., & Meunier, P. (2016). The mass balance of earthquakes and earthquake sequences. *Geophysical Research Letters*, *43*, 3708–3716. https://doi.org/10.1002/2016GL068333

Marc, O., Hovius, N., Meunier, P., Gorum, T., & Uchida, T. (2016). A seismologically consistent expression for the total area and volume of earthquake-triggered landsliding. *Journal of Geophysical Research: Earth Surface*, *121*, 640–663. https://doi.org/10.1002/2015JF003732.Received

Marlow, M. S., Gardner, J. V., & Normark, W. R. (2000). Using high-resolution multibeam bathymetry to identify seafloor surface rupture along the Palos Verdes fault complex in offshore southern California. *Geology*, *28*(7), 587–590. https://doi.org/10.1130/0091-7613(2000)28<587:UHMBTI>2.0.CO;2

Masson, D. G., Harbitz, C. B., Wynn, R. B., Pedersen, G., & Løvholt, F. (2006). Submarine landslides: Processes, triggers and hazard prediction. P*hilosophical Transactions of the Royal Society of London. Series A*, *364*(1845), 2009–2039. https://doi.org/10.1098/rsta.2006.1810

Mazzanti, P., & De Blasio, F. V. (2013). The dynamics of subaqueous rock avalanches: The role of dynamic fragmentation. *Landslide Science and Practice*. https://doi.org/10.1007/978-3-642-31427-8_4

McAllister, E., & Cann, J. R. (1996). Initiation and evolution of boundary-wall faults along the Mid-Atlantic Ridge, 25–29°N, *Geological Society Special Publication*, *118*, 29–48. https://doi.org/10.1144/GSL.SP.1996.118.01.03

McLeod, A. E., & Underhill, J. R. (1999). Processes and products of footwall degradation, northern Brent Field, Northern North Sea. *Petroleum Geology Conference Proceedings*, *5*, 91–106. https://doi.org/10.1144/0050091

Migeon, S., Cattaneo, A., Hassoun, V., Larroque, C., Corradi, N., Fanucci, F., et al. (2011). Morphology, distribution and origin of recent submarine landslides of the Ligurian Margin (North-western Mediterranean): Some insights into geohazard assessment. *Marine Geophysical Researches*, *32*(1), 225–243. https://doi.org/10.1007/s11001-011-9123-3

Mitchell, N. C. (2005). Interpreting long-profiles of canyons in the USA Atlantic continental slope. *Marine Geology*, *214*(1–3), 75–99. https://doi.org/10.1016/j.margeo.2004.09.005

Mitchell, N. C., Dade, W. B., & Masson, D. G. (2003). Erosion of the submarine flanks of the Canary Islands. *Journal of Geophysical Research*, *108*(F1). 6002. https://doi.org/10.1029/2002jf000003

Mitchell, N. C., Tivey, M. A., & Gente, P. (2000). Seafloor slopes at mid-ocean ridges from submersible observations and implications for interpreting geology from seafloor topography. *Earth and Planetary Science Letters*, *183*(3–4), 543–555. https://doi.org/10.1016/S0012-821X(00)00270-3

Moernaut, J., Daele, M. V., Heirman, K., Fontijn, K., Strasser, M., Pino, M., et al. (2014). Lacustrine turbidites as a tool for quantitative earthquake reconstruction: New evidence for a variable rupture mode in south central Chile. *Journal of Geophysical Research: Solid Earth*, *119*, 1607–1633. https://doi.org/10.1002/2013JB010738

Mosher, D. C., Piper, D. J. W., Calvin Campbell, D., & Jenner, K. A. (2004). Near-surface geology and sediment-failure geohazards of the central Scotian Slope. *Bulletin*, *88*(6), 703–723. https://doi.org/10.1306/01260403084

Mountjoy, J. J., Howarth, J. D., Orpin, A. R., Barnes, P. M., Bowden, D. A., Rowden, A. A., et al. (2018). Earthquakes drive large-scale submarine canyon development and sediment supply to deep-ocean basins. *Science Advances*, *4*(3). https://doi.org/10.1126/sciadv.aar3748

Olive, J.-A., Parnell-Turner, R., Escartín, J., Smith, D. K., & Petersen, S. (2019). Controls on the seafloor exposure of detachment fault surfaces. *Earth and Planetary Science Letters*, *506*, 381–387. https://doi.org/10.1016/j.epsl.2018.11.001

Orange, D. L., McAdoo, B. G., Casey Moore, J., Tobin, H., Screaton, E., Chezar, H., et al. (1997). Headless submarine canyons and fluid flow on the toe of the Cascadia accretionary complex. *Basin Research*, *9*(4), 303–312. https://doi.org/10.1046/j.1365-2117.1997.00045.x

Pelletier, J. D., DeLong, S. B., Al-Suwaidi, A. H., Cline, M., Lewis, Y., Psillas, J. L., & Yanites, B. (2006). Evolution of the Bonneville shoreline scarp in west-central Utah: Comparison of scarp-analysis methods and implications for the diffusion model of hillslope evolution. *Geomorphology*, *74*(1–4), 257–270. https://doi.org/10.1016/j.geomorph.2005.08.008

Petit, C., Gunnell, Y., Gonga-Saholiariliva, N., Meyer, B., & Séguinot, J. (2009). Faceted spurs at normal fault scarps: Insights from numerical modeling. *Journal of Geophysical Research*, *114*(5), B05403. https://doi.org/10.1029/2008JB005955

Petit, C., & Mouthereau, F. (2012). Steep topographic slope preservation by anisotropic diffusion: An example from the Neogene Têt fault scarp, eastern Pyrenees. *Geomorphology*, *171–172*, 173–179. https://doi.org/10.1016/j.geomorph.2012.05.016

Phillips, F. M., Ayarbe, J. P., Harrison, J. B. J., & Elmore, D. (2003). Dating rupture events on alluvial fault scarps using cosmogenic nuclides and scarp morphology. *Earth and Planetary Science Letters*, *215*(1–2), 203–218. https://doi.org/10.1016/S0012-821X(03)00419-9

Puga-Bernabéu, Á., Webster, J. M., Beaman, R. J., & Guilbaud, V. (2011). Morphology and controls on the evolution of a mixed carbonate-siliciclastic submarine canyon system, Great Barrier Reef margin, north-eastern Australia. *Marine Geology*, *289*(1–4), 100–116. https://doi.org/10.1016/j.margeo.2011.09.013

Roering, J. J., Kirchner, J. W., & Dietrich, W. E. (1999). Evidence for nonlinear, diffusive sediment transport on hillslopes and implications for landscape morphology. *Water Resources Research*, *35*(3), 853–870. https://doi.org/10.1029/1998WR900090

Rosenbloom, N. A., & Anderson, R. S. (1994). Hillslope and channel evolution in a marine terraced landscape, Santa Cruz, California. *Journal of Geophysical Research*, *99*(B7). https://doi.org/10.1029/94jb00048

Salichon, J., Lemoine, A., & Aochi, H. (2009). Validation of teleseismic inversion of the 2004 Mw 6.3 Les Saintes, Lesser Antilles, earthquake by 3D finite-difference forward modeling. *Bulletin of the Seismological Society of America*, *99*(6), 3390–3401. https://doi.org/10.1785/0120080315

Sanchez, G., Rolland, Y., Corsini, M., Braucher, R., Bourlès, D., Arnold, M., & Aumaître, G. (2010). Relationships between tectonics, slope instability and climate change: Cosmic ray exposure dating of active faults, landslides and glacial surfaces in the SW Alps. *Geomorphology*, *117*(1–2), 1–13. https://doi.org/10.1016/j.geomorph.2009.10.019

Schwanghart, W., & Scherler, D. (2014). Short Communication: TopoToolbox 2 - MATLAB-based software for topographic analysis and modeling in Earth surface sciences. *Earth Surface Dynamics*, *2*(1), 1–7. https://doi.org/10.5194/esurf-2-1-2014

Searle, R. C., & Escartín, J. (2004). The rheology and morphology of oceanic lithosphere and mid-ocean ridges. *Geophysical Monograph Series*, *148*. https://doi.org/10.1029/148GM03

Stewart, S. A., & Reeds, A. (2003). Geomorphology of kilometer-scale extensional fault scarps: Factors that impact seismic interpretation. *Bulletin*, *87*(2), 251–272. https://doi.org/10.1306/08190201041

Strasser, M., Anselmetti, F. S., Fäh, D., Giardini, D., & Schnellmann, M. (2006). Magnitudes and source areas of large prehistoric northern Alpine earthquakes revealed by slope failures in lakes. *Geology*, *34*(12), 1005–1008. https://doi.org/10.1130/G22784A.1

Tucholke, B. E. (1992). Massive submarine rockslide in the rift-valley wall of the Mid-Atlantic Ridge. *Geology*, *20*(2), 129–132. https://doi.org/10.1130/0091-7613(1992)020<0129:MSRITR>2.3.CO;2

Tucholke, B. E., Kenneth Stewart, W., & Kleinrock, M. C. (1997). Long-term denudation of ocean crust in the central North Atlantic Ocean. *Geology*, *25*(2), 171–174. https://doi.org/10.1130/0091-7613(1997)025<0171:LTDOOC>2.3.CO;2

Tucker, G. E., Hobley, D. E. J., McCoy, S. W., & Struble, W. T. (2020). Modeling the Shape and Evolution of Normal-Fault Facets. *Journal of Geophysical Research: Earth Surface*, *125*, e2019JF005305. https://doi.org/10.1029/2019JF005305

Tucker, G. E., McCoy, S. W., Whittaker, A. C., Roberts, G. P., Lancaster, S. T., & Phillips, R. (2011). Geomorphic significance of postglacial bedrock scarps on normal-fault footwalls. *Journal of Geophysical Research*, *116*(1), F01022. https://doi.org/10.1029/2010JF001861

Van Daele, M., Moernaut, J., Doom, L., Boes, E., Fontijn, K., Heirman, K., et al. (2015). A comparison of the sedimentary records of the 1960 and 2010 great Chilean earthquakes in 17 lakes: Implications for quantitative lacustrine palaeoseismology. *Sedimentology*, *62*(5), 1466–1496. https://doi.org/10.1111/sed.12193

Varnes, D. (1978). *Slope movement types and processes. Transportation Research Board Special Report (Report No. 176)*.

Wallace, R. E. (1977). Profiles and ages of young fault scarps, north-central Nevada. *Geological Society of America Bulletin*, *88*(9), 1267–1281. https://doi.org/10.1130/0016-7606(1977)88<1267:PAAOYF>2.0.CO;2

Wallace, R. E. (1978). Geometry and rates of change of fault-generated range front, north-central {Nevada}. *Journal of Research of the U. S. Geological Survey*, *6*(5), 637–650.

Weatherall, P., Marks, K. M., Jakobsson, M., Schmitt, T., Tani, S., Arndt, J. E., et al. (2015). A new digital bathymetric model of the world's oceans. *Earth and Space Science*, *2*(8), 331–345. https://doi.org/10.1002/2015ea000107

Weber, J. C., Dixon, T. H., DeMets, C., Ambeh, W. B., Jansma, P., Mattioli, G., et al. (2001). GPS estimate of relative motion between the Caribbean and South American plates, and geologic implications for Trinidad and Venezuela. *Geology*, *29*(1), 75–78. https://doi.org/10.1130/0091-7613(2001)029<0075:GEORMB>2.0.CO;2

Whipple, K. X., & Tucker, G. E. (1999). Dynamics of the stream-power river incision model: Implications for height limits of mountain ranges, landscape response timescales, and research needs. *Journal of Geophysical Research*, *104*(B8), 17661–17674. https://doi.org/10.1029/1999jb900120

Wobus, C., Whipple, K. X., Kirby, E., Snyder, N., Johnson, J., Spyropolou, K., et al. (2006). Tectonics from topography: Procedures, promise, and pitfalls. *Special Paper of the Geological Society of America*, *398*(04), 55–74. https://doi.org/10.1130/2006.2398(04

Zami, F., Quidelleur, X., Ricci, J., Lebrun, J.-F., & Samper, A. (2014). Initial sub-aerial volcanic activity along the central Lesser Antilles inner arc: New K-Ar ages from Les Saintes volcanoes. *Journal of Volcanology and Geothermal Research*, *287*, 12–21. https://doi.org/10.1016/j.jvolgeores.2014.09.011